MIT Libraries | DSpace@MIT

MIT Open Access Articles

Interplay between elastic instabilities and shear-banding: three categories of Taylor–Couette flows and beyond

Massachusetts Institute of Technology

Interplay between elastic instabilities and shear-banding:
Three categories of Taylor-Couette flows and beyond

M.A. Fardin,[1,2,3] T.J. Ober,[2] V. Grenard,[4] T. Divoux,[4] S. Manneville,[4,5] G.H. McKinley,[2] and S. Lerouge[1,3,*]

[1]*Laboratoire Matière et Systèmes Complexes, CNRS UMR 7057*
Université Paris Diderot, 10 rue Alice Domont et Léonie Duquet, 75205 Paris Cédex 13, France
[2]*Department of Mechanical Engineering*
Massachusetts Institute of Technology, 77 Massachusetts Avenue, MA 02139-4307 Cambridge, USA
[3]*The Academy of Bradylogists*
[4]*Université de Lyon, Laboratoire de Physique, CNRS UMR 5672*
École Normale Supérieure de Lyon, 46 Allée d'Italie, 69364 Lyon cedex 07, France
[5]*Institut Universitaire de France*
(Dated: July 20, 2012)

In the past twenty years, shear-banding flows have been probed by various techniques, such as rheometry, velocimetry and flow birefringence. In micellar solutions, many of the data collected exhibit unexplained spatiotemporal fluctuations. Recently, it has been suggested that those fluctuations originate from a purely elastic instability of the shear-banding flow. In cylindrical Couette geometry, the instability is reminiscent of the Taylor-like instability observed in viscoelastic polymer solutions. The criterion for purely elastic Taylor-Couette instability adapted to shear-banding flows suggested three categories of shear-banding depending on their stability. In the present study, we report on a large set of experimental data which demonstrates the existence of the three categories of shear-banding flows in various surfactant solutions. Consistent with theoretical predictions, increases in the surfactant concentration or in the curvature of the geometry destabilize the flow, whereas an increase in temperature stabilizes the flow. But experiments also exhibit some interesting behaviors going beyond the purely elastic instability criterion.

Introduction

In 1991, Rehage and Hoffmann wrote a seminal review article entitled: "Viscoelastic surfactant solutions: model systems for rheological research" [1]. More than twenty years later, their point is still vividly accurate. One could even argue that throughout the years, studies around surfactant solutions have reflected some of the new developing trends in rheological research. (1) The original focus was on scaling laws of "living polymers" and their surprisingly robust Maxwellian behavior at small deformations. (2) The focus then shifted toward the shear-banding transition observed in nonlinear rheology. (3) Nowadays researchers are also concerned with the stability of such banded flows, in particular with respect to elastic instabilities.

Surfactant solutions can have a variety of mesoscopic structures at equilibrium: vesicles, rods, entangled or connected worms, liquid crystals or lamellar phases [2, 3]. Rehage and Hoffmann's review focused on surfactant molecules possessing packing properties which favor the formation of cylindrical micelles, sometimes with the help of added salt [1, 4]. They described how, in semi-dilute and concentrated regimes, wormlike micelles are entangled as in polymer solutions. In comparison to solutions of polymers, there is, however, one important difference. The permanent exchange of surfactant molecules

leads to the perpetual breaking and reformation of the worms. This is why they are sometimes called "living polymers". Stress relaxation is modified by this additional mechanism, in a way modelled efficiently by Cates' reptation-reaction model [5]. Strikingly, this added complexity at the mesoscopic scale leads to simpler macroscopic properties. Indeed, in polymer solutions, polydispersity in the chain lengths generates a range of relaxation times, whereas, for wormlike micelles, if the breaking processes are fast in contrast to reptation, the average length of worms dominates and the stress relaxation is mono-exponential [5]. We shall come back on the linear rheology of solutions of wormlike micelles in the first section of this paper.

If the variety of structures present in surfactant solutions at equilibrium is already very rich, the range of shear-induced structures (out of equilibrium) is even greater, and far less understood [4]. By investigating the nonlinear rheology of wormlike micellar solutions, Rehage and Hoffman gave the first robust experimental observation of what was then to be coined "shear-banding" [1]. Roughly speaking, a shear-banding transition is reminiscent of a first order phase transition [6–12]. Above a critical shear rate $\dot{\gamma}_l$, the shear stress plateaus at a value σ_p. Then, up to a second higher critical shear rate $\dot{\gamma}_h$, the flow is inhomogeneous, split in two bands with different structures and local shear rates $\dot{\gamma}_l$ and $\dot{\gamma}_h$. To leading order, for $\dot{\gamma} \in [\dot{\gamma}_l, \dot{\gamma}_h]$, an increase in the value of the macroscopic shear rate $\dot{\gamma}$ only increases the proportion $\alpha \in [0, 1]$ of the high shear rate band, following a 'simple lever rule' $\dot{\gamma} \simeq \alpha \dot{\gamma}_h + (1 - \alpha) \dot{\gamma}_l$. This scenario has been confirmed experimentally with various techniques like pure viscom-

etry, velocimetry, birefringence, *etc.* (see [13] and Ref. therein) and we shall highlight typical observations in the first section of the present paper.

The simple lever rule scenario of shear-banding phenomenon was roughly confirmed in the last twenty years [14, 15], but many unexpected fluctuating behaviours were observed in all the gathered data [15–19, 25]. Thus, in the last few years, the focus shifted toward the stability of shear-banded flows and the importance of elastic instability mechanisms potentially triggering secondary flows (laminar or turbulent) responsible for the fluctuations on the main flow [5, 26, 27, 29, 30, 33, 35–38].

In order to show, first, the existence of secondary flows and, second, their elastic origin, we conducted, in previous studies, intensive experiments on two systems: a 11 wt % semi-dilute aqueous mixture of cetyltrimethylammonium bromide (CTAB; 0.3 M) and sodium nitrate (NaNO$_3$; 0.405 M) at a temperature $T = 28°$C [35–38], and a 10 wt % cetylpyridinium chloride (CPCl; 0.238 M) and sodium salicylate (NaSal; 0.119 M) in NaCl brine at $T = 21.5°$C [39]. In both cases, the shearing geometry was a Taylor-Couette (TC) device with a gap $d = 1.13$ mm and an inner rotating cylinder of radius $R_i = 13.33$ mm. Both series of experiments confirmed the presence of secondary flows on top of a primary shear-banding flow. Those secondary flows originated from an instability of the material constituting the high shear rate band and thus also filling the entire geometry for $\dot{\gamma} > \dot{\gamma}_h$. But the successions of secondary flows in the two systems were different. Our analysis suggested that this difference may be due to subtle changes in boundary conditions on the unstable domain [38]. Indeed, in a recent theoretical letter where we derived the appropriate dimensionless group controlling the threshold to elastic instability in shear-banded flows, we predicted the existence of three categories of shear-banding flows, depending on their stability [stable SB, unstable SB (3D coherent) or unstable SB (3D coherent then turbulent)] [40]. The two systems investigated so far seemed to validate the existence of the two unstable categories of shear-banding, while the third category–stable shear-banding flow–was left to be witnessed experimentally.

In the present study, we vastly increase the volume of data supporting the emerging rationale behind the instability of shear-banded flows. We report on a large set of experimental data which demonstrates the existence of the three categories of shear-banding flows, essentially for one surfactant system in various thermodynamical and geometrical conditions. Consistent with theoretical predictions [40], increases in the concentration of surfactant or in the curvature of the geometry destabilize the flow, whereas an increase in temperature stabilizes the flow.

The paper is organized as follows. In section I, we highlight the preparation of the various samples and the different experimental techniques employed. This section is also used to recall some classical results concerning: (1) the scaling laws of "living polymers" and their robust Maxwellian behavior under small deformations; and (2) typical observations of the base shear-banding flow. Section II is concerned with (3) the stability of shear-banding flows. It summarizes the observations collected on the model system of CTAB/NaNO$_3$ for various surfactant or salt concentrations, various temperatures and various geometries of the TC device. We recall the theoretical arguments suggesting the existence of three categories of shear-banding flows and we show robust evidences for them. In section III, we discuss phenomena that can become relevant when one explores extreme values of temperature or concentrations or when one departs from the small gap regime. All of those cases go beyond the simple theory we developed recently. Finally, we conclude in section IV.

I. MATERIALS, METHODS AND PRELIMINARY RESULTS

1. Samples

The main goal of this study is to demonstrate the the existence and the robustness of the three categories of shear-banding flows that we have recently predicted. Therefore, we have conducted experiments on a very large range of solutions. In section II, we describe results for various semi-dilute and concentrated aqueous mixture of cetyltrimethylammonium bromide (CTAB) and sodium nitrate (NaNO$_3$). In order to be consistent with the literature [42], we have used solutions of 0.3 M of CTAB with salt concentrations varying between 0.1 M and 2.8 M. We have also used solutions with 0.3 M of NaNO$_3$ and with surfactant concentrations varying between 0.1 M and 0.7 M, allowing to widely explore the semi-dilute regime but also the concentrated regime. Experiments for varying concentrations of salt or surfactant were conducted at $T=30°$C in a TC geometry with $d = 1.13$ mm and $R_i = 13.33$ mm. Experiments for varying temperatures or for varying geometries were conducted on a sample of 0.3 M of CTAB and 0.4 M of NaNO$_3$. Temperatures were taken between the Krafft temperature ($T \simeq 21.5°$C) and 40°C [42]. Below the Krafft temperature, the surfactant is not soluble in water.

In addition to the systematic variation of the thermodynamical parameters for the CTAB/NaNO$_3$ system, we also probed other systems. Hence a few data in the manuscript concern the concentrated 20% CTAB/D$_2$O solution [18–22] and the semi-dilute 10% CPCl/NaSal/brine system [15–17, 24, 25, 39].

All samples were made at least two weeks before experiments and were stored in the dark at 35°C.
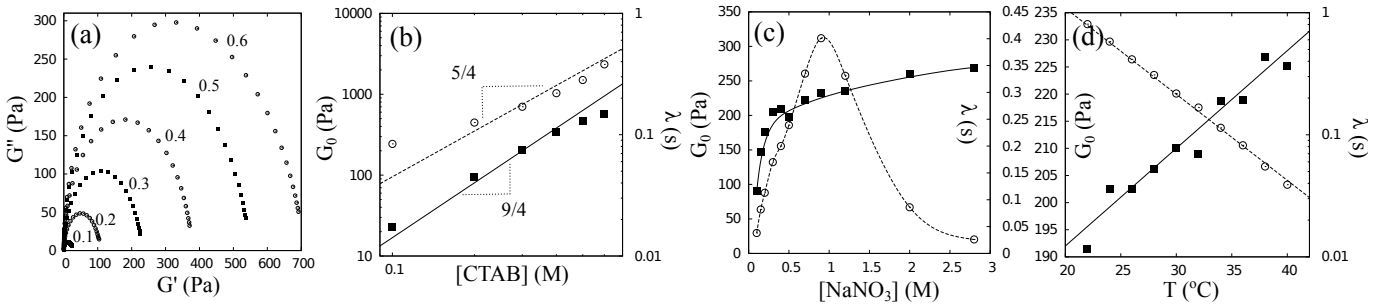
FIG. 1: Linear rheology of solutions of CTAB/NaNO$_3$. (a) Example of semi-circular Cole-Cole plots showing the Maxwellian behavior of wormlike micelles solutions. The storage and loss moduli (G' and G'') were obtained from small amplitude oscillatory tests in cone-and-plate geometry for solutions with [NaNO$_3$]=0.3 M at T=30°C. The concentrations of CTAB are given directly on the figure (in M). We have also performed linear rheology in small gap TC geometry and the data are identical. (b-d) Summary of the relaxation times (○, right axis) and elastic moduli (■, left axis) as functions of (b) the surfactant concentration [CTAB] for fixed salt concentration ([NaNO$_3$]=0.3 M) and temperature (T=30°C); (c) the salt concentration [NaNO$_3$] for fixed surfactant concentration ([CTAB]=0.3 M) and temperature (T=30°C); (d) the temperature T for fixed salt and surfactant concentrations ([CTAB]=0.3 M and [NaNO$_3$]=0.4 M). In (c), the lines are guides to the eye. In all other cases, they are theoretical fits discussed in the text.

2. Shearing geometries

All the experiments were performed in transparent cylindrical Couette devices with smooth walls, also referred to as TC cells in the following. In all experiments, only the inner cylinder was rotating and its axis was adapted to a stress-controlled rheometer (Physica MCR301). The top of the cell was closed by a small plug which limits the destabilization of the free surface of the fluid at high shear rates [36] and a home-made solvent trap was also used to limit evaporation. In order to check for the effect of higher curvature of the streamlines on the onset of elastic instability, we used various inner and outer radii. We used two types of outer radii, R_o = 14.46 or 25 mm. With the large outer radius, we used two types of inner radii R_i = 13.33 or 24 mm. With the smaller outer radius, we also used two types of inner radii R_i = 11.97 or 13.33 mm. All cylinders are H = 40 mm high.

In the following, shearing geometries will be referred to using the two dimensionless ratios defined as $\Lambda \equiv d/R_i$ and $\Gamma \equiv d/H$. Overall we have four TC devices, with $\Lambda \simeq 0.04, 0.08, 0.2$ and 0.9 ($\Gamma \simeq 0.025, 0.025, 0.06, 0.3$). Note that in addition to the TC geometries, a cone-and-plate device (radius 25 mm, angle 1°) was used for linear rheology and measurement of a few flow curves. Moreover, to test inertial effects, we used a transparent cylindrical double-gap geometry, that consists in an inner cylinder with a shape of a hollow cylinder mounted in the center of the outer fixed cylinder. Consequently, the inner cylinder presents both an inner and outer surface leading to a double-gap configuration : the inner gap has a rotating outer cylinder and a rotating inner cylinder while the situation is the opposite for the outer gap. Details on the double-gap device are given in ESI.

3. Linear rheology

Small amplitude oscillatory tests [2, 41] were conducted (both in TC and in cone-and-plate geometries) on all samples in order to extract their elastic modulus G_0 and relaxation time λ from Maxwellian fits of the storage and loss moduli (G' and G'') [42]. Fig. 1a gives, as an example, the Cole-Cole plots for varying concentrations of CTAB at constant salt concentration and temperature. The semi-circular shapes confirm the Maxwellian behavior of the solutions in the linear rheology regime. Overall, all of the linear rheology data collected are consistent with the literature [42]. Fig. 1b, c and d give the variations of G_0 and λ as functions of the surfactant concentration, the salt concentration and temperature. We have $G_0 \sim$[CTAB]$^{9/4}$ and $\lambda \sim$[CTAB]$^{5/4}$, as expected from Cates's reptation-reaction model [5, 42]. Also expected are the Arrhenius equation for the relaxation time as a function of temperature, and the linear relation between the elastic modulus and temperature $G_0 = k_B T/\xi^3$, where k_B is the Boltzmann constant and ξ is the mesh size of the entanglement network [5]. The variations of λ and G_0 with the concentration of salt [NaNO$_3$] are consistent with the literature [42]. The initial increase of λ and G_0 with [NaNO$_3$] is generally admitted to be a consequence of the screening of electrostatic interactions, which induces micellar growth [5, 42]. The subsequent decrease of λ at higher salt concentration is supposed to reflect the effect of micellar branching [5, 42].

4. Nonlinear rheology

Although in the regime of small deformations the Maxwell model is sufficient to account for the rheology of the solutions, it becomes completely inadequate in the
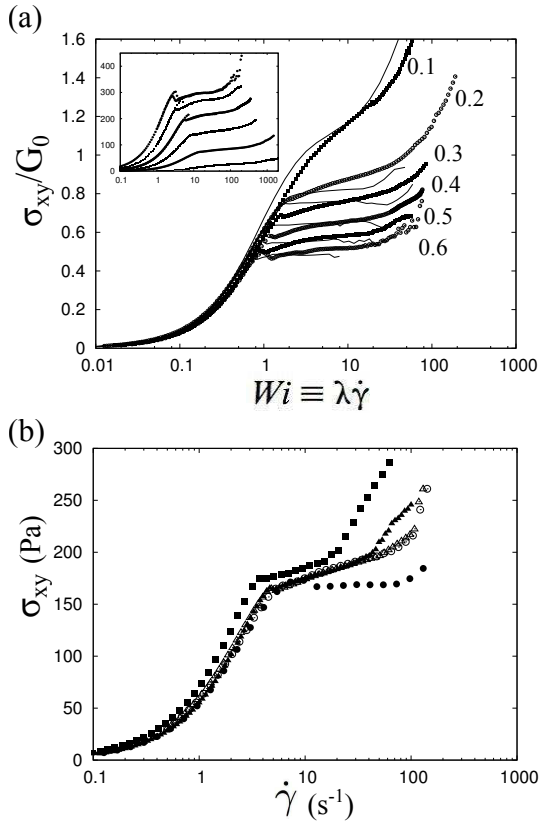
FIG. 2: (a) Experimental flow curves obtained for various concentrations of [CTAB]=0.1, 0.2, 0.3, 0.4, 0.5 and 0.6 M at a constant salt concentration [NaNO$_3$]=0.3 M and constant temperature T=30°C. The flow curves were obtained by increasing the imposed shear rate. The shear stress is in units of G_0 and the shear rate is made dimensionless by using the Weissenberg number $Wi \equiv \lambda\dot{\gamma}$. The flow curves with the symbols (■ and ○) were obtained on a TC device with $d = 1.13$ mm and $R_i = 13.33$ mm, with two minutes spent on each data point. The continuous lines are the corresponding flow curves obtained in cone-and-plate geometry (2 min/point). Inset: TC flow curves in dimensional form (σ_{xy} vs $\dot{\gamma}$), stacked from top to bottom in between [CTAB]=0.6 M and [CTAB]=0.1 M. For each system, two runs are plotted, one with a sampling time of 2 min/point (corresponding to the dimensionless data) and one with only 5 s/point. (b) Experimental flow curves for a system with [CTAB]=0.3 M, [NaNO$_3$]=0.4 M and T=28°C. The flow curves are obtained in different shearing geometries: cone-and-plate (●) and TC with Λ =0.04 (○), 0.08 (△), 0.2 (▲) and 0.9 (■); 2 min/point.

nonlinear regime. The crossover between the linear and nonlinear rheology regime can be roughly given by the Weissenberg number. The Weissenberg number is defined as $Wi \equiv \lambda\dot{\gamma}$ [46]. For $Wi \ll 1$ the rheology is linear and the solutions behave as Maxwellian fluids. For $Wi \gtrsim 1$ the solutions exhibit shear-banding or at least shear-thinning [4].

Fig. 2a gives, as an example, the flow curves for varying concentrations of CTAB at constant salt concentration and temperature. When the global shear stress σ_{xy} is directly plotted against the global shear rate $\dot{\gamma}$ (inset), flow curves are stacked, with shear-banding plateaus at higher stresses and spanning a smaller range of shear rates corresponding to the more concentrated solutions. This follows from the rough scaling $\sigma_p \sim G_0$ and $\dot{\gamma}_l \sim \lambda^{-1}$. If flow curves are made dimensionless by plotting σ_{xy}/G_0 against Wi we can see that indeed all stress plateaus start for $Wi \simeq 1$ [4]. The dimensionless curves are stacked the other way round: the solutions with a higher surfactant concentration have a lower and wider dimensionless plateau [4]. The existence of a plateau on the flow curve is the mechanical signature of shear-banding. For the lowest concentration of surfactant ([CTAB]=0.1 M), the dimensionless flow curve does not have a plateau and shear-banding does not occur. The flow curves in Fig. 2a are consistent with the literature [42], and we checked that it was also the case for the flow curves for varying temperatures and salt concentrations (see ESI) and for other surfactants [8, 20]. In general, we can define the apparent Weissenberg number marking the end of the shear-banding plateau as $Wi_h^* \equiv \lambda\dot{\gamma}_h^*$, where $\dot{\gamma}_h^*$ is the apparent end of the plateau. Then, Fig. 2a seems to show that Wi_h^* increases with the surfactant concentration [4, 40]. We also observed a similar increase of Wi_h^* with decreasing temperature (see ESI). For varying salt concentrations the effect on Wi_h^* is more subtle. The variations of σ_p/G_0 and Wi_h^* with [NaNO$_3$] are non-monotonic. Consistently with ref. [42] (Fig. 9), we found roughly three domains. First, σ_p/G_0 increases, for concentrations up to [NaNO$_3$] $\simeq 0.5$ M, then levels off for concentrations up to [NaNO$_3$] $\simeq 1$ M. Finally, for [NaNO$_3$] > 1 M, σ_p/G_0 decreases (see ESI). This will be discussed further in sections II E and III C.

As a transition to the next subsection, let us mention a point that we believe to be essential in analysing flow curves: the data collected in experiments very rarely correspond to the ideal conditions of a steady simple shear flow, the very conditions most of the time assumed in modelling, that is without secondary flows and without wall slip.

On steadiness, the well-known kinetics of the establishment of banded flows can be particularly slow, especially near the beginning of the shear-banding regime, when $\alpha \ll 1$ [4, 13, 47]. The time spent on each data point of the flow curve must be greater than the time needed to reach the steady state. In the inset of Fig. 2a, we have plotted two runs for each flow curves. One with a time sampling of 2 min/point and one with a sampling of 5 s/point. Note how at the beginning of the plateau, the shorter sampling produces higher stresses because not enough time was allowed to reach steady state. It is a phenomenon long known to happen in shear-banding fluids [4, 13].

The presence of slip at the walls, *i.e.* a mismatch between the velocity of the fluid adjacent to the wall and of the wall itself, also impacts the flow curve. The true shear

rate experienced by the bulk of the sample is smaller than the imposed shear rate, leading to a shift of the stress plateau towards lower global shear rates. The position of the stress plateau and its width may also be affected. For more details on wall slip, please see section I 5.

It is also important to realize that in cylindrical geometries, the stress is not homogeneous in the gap but decreases as $1/r^2$ [36, 41]. This is one of the reasons why the shear-banding plateaus measured in TC devices are tilted in contrast to those measured in cone-and-plate [36, 48–50]. But it is not the only reason. Fig. 2b gives five flow curves for the same surfactant system ([CTAB]=0.3 M, [NaNO$_3$]=0.4 M, T=28°C) but obtained in different shearing geometries. As noticed in a previous publication [36], the slope of the stress plateau is not simply related to the curvature of the geometry. For instance, TC devices with $\Lambda \simeq 0.04$, 0.08, 0.2 have almost exactly the same slope. The slope of the plateau may also be influenced by a concentration difference between the bands [51].

Most importantly, Fig. 2b illustrates the fact that the shape of the flow curves can be greatly influenced by secondary flows. For $\Lambda = 0.2$ and 0.9 the flows become turbulent before the end of the shear banding regime (for $\alpha < 1$) and the apparent upper branch of the flow curves is due to the strong extra stress generated by turbulent flows. This point was discussed in detail in a recent publication [39]. In this case, the apparent end of the stress plateau Wi_h^* is not the *true* end, *i.e.* such that $\alpha = 1$.

Although the plateaus measured in cone-and-plate geometry do not seem to have a slope, it does not mean that secondary flows are absent. Indeed, in Fig. 2a data collection usually had to be stopped due to the ejection of the sample, mostly triggered by secondary flows as already mentioned in a previous publication [40] and as explicitly shown in a recent study [52].

5. Observing secondary flows

Almost all experiments presented in this article have been performed in a rheo-optical device where the gap of the TC device was visualized by using a laser sheet (wavelength 632.8 nm) propagating along the velocity gradient axis and extending along the vorticity axis. A digital camera recorded the scattered intensity at 90°, giving a view of the gap in the velocity-gradient/vorticity (y, z) plane [36]. Fig. 3a (ii) gives an example of the type of images gathered. For most solutions, the turbidity contrast between the bands was strong enough that we could clearly see the interface between the bands. We then applied a numerical algorithm to each frame in order to detect the interface [36, 37]. We have also imaged the gap with white light in order to observe the vortex structure [37], even when the turbidity contrast is weak. The evolution in space and time of the amplitude of the interface along z has been shown previously to be correlated to secondary flows [37]. When the interface exhibits un-

dulations, each wavelength of the interface corresponds to a pair of counter-rotating Taylor-like vortices, mainly localized in the high shear rate band, with inward flows co-localized with the interface inner crests and outward flows co-localized with the interface outer crests. The size of a pair of vortices is symbolized by $2L$. A precise description of the TC devices used for optical visualisations is given elsewhere [36, 37] and in the Electronic Supplementary Information (ESI).

Evidently, due to incompressibility, velocity components involved in secondary flows locally modify the base flow $v_\theta(y, z)$. In order to check this fact, we have performed velocity measurements using the ultrasonic velocimetry (USV) set-up described in detail elsewhere [53]. Typical velocity profiles $v_\theta(y)$ measured at a particular location along z are given in Fig. 3c for the solution [CTAB]=0.3 M, [NaNO$_3$]=0.4 M at T=28° C in a TC cell with $\Lambda \simeq 0.08$. They exhibit the characteristic profile broken in two slopes corresponding to the high and low shear rates bands [13]. As shown in Fig. 3d, the proportion of the high shear rate band α increases roughly linearly with the global shear rate $\dot{\gamma}$, as measured consistently by both velocimetry and optical methods.

We have demonstrated in a previous study how the spatio-temporal dynamics of the secondary flows and thus of the interface as imaged by turbidity contrast are related to the dynamics of velocity profiles of the base flow $v_\theta(y)$ [39]. Fig 3a (i) and Fig 3b now show how the vorticity structuring of secondary flows modifies measurements of velocity profiles done at several consecutive locations along the vorticity axis. The position of the interface between the two shear bands clearly undulates along the vertical direction, demonstrating the full consistency between the optical and velocimetry measurements.

The velocity measurements also reveal the presence of systematic apparent slip at the wall in contact with the high shear rate band. As shown in Fig 3e, the slip velocity first increases at the beginning of the shear-banding regime and then levels off at a value of a few mm/s. A similar evolution of the local shear rate in the high shear rate band is observed as shown in Fig 3.f. Indeed, in contrast with the expectations of the simple lever rule, the high shear rate $\dot{\gamma}_h$ is not constant throughout the entire shear-banding regime. It first increases and then tends to saturate to a value $\dot{\gamma}_h$=89± 4 s^{-1} consistent with the end of the plateau [$\dot{\gamma}_h^*$=97± 5 s^{-1} (Fig. 2.b)] (this last observation is robust as long as the shear-banding flow does not become turbulent, depending on the value of Λ). All these features are consistent with our previous investigation of the 10% CPCl/NaSal solution [39] and seem to be widespread across shear-banding micellar systems [19, 43–45].

In the rest of this article, we will assume that this phenomenology–wall slip correlated with a gradual increase of $\dot{\gamma}_h(\dot{\gamma})$–is systematic. We will discuss its overall impact on secondary flows and on their onset in section III A.

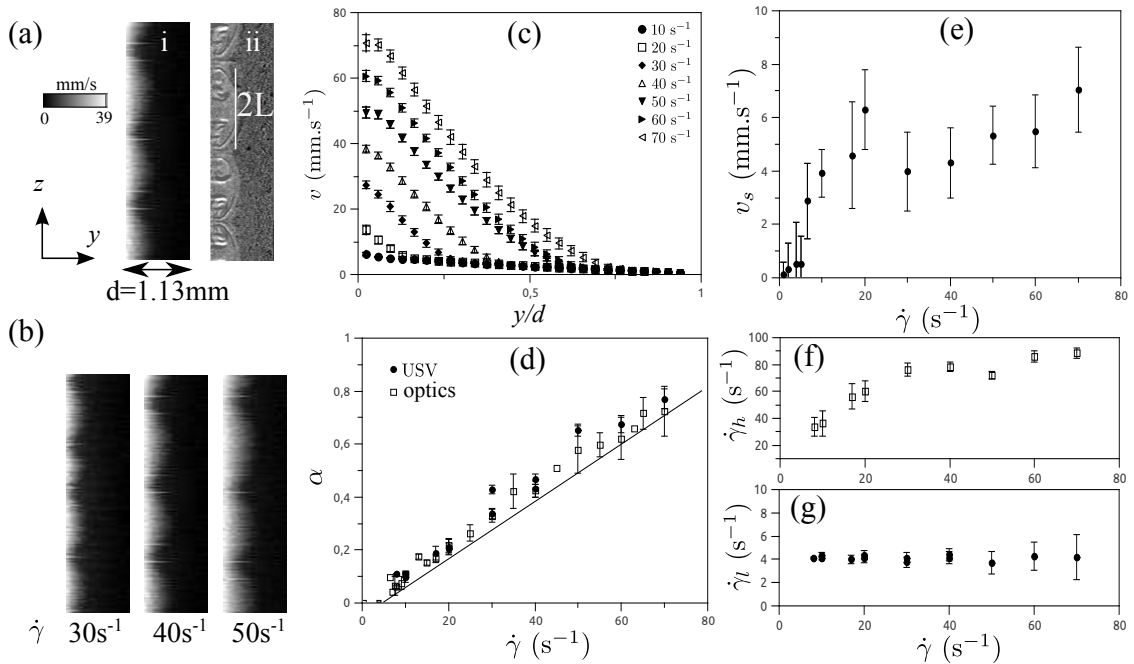Most of the experimental results presented in this pa-

FIG. 3: (a) Comparison between (i) velocity measurements and (ii) optical visualizations of the shear-banding flow of a solution of [CTAB]=0.3 M, [NaNO$_3$]=0.4 M, T=28°C, $\Lambda \simeq 0.08$, at $\dot{\gamma} = 40$ s^{-1}. (i) USV measurements. Each horizontal line is a velocity profile $v_\theta(y)$ at a given location z along the vorticity axis, with the velocity encoded as a grey level between the zero velocity at the fixed outer cylinder (right) and v_w=39 mm/s, the velocity at the moving inner cylinder (left). Measurements along z were done every 100 μm, which is above the vertical resolution of the transducer (65 μm). The time interval between each velocity profile is between 0.5 and 1 s depending on the applied shear rate. (ii) Overlay of two optical visualization techniques showing the secondary vortex flow in the high shear rate band. The first technique, with the red laser, gives the strong turbidity contrast between the bands. The second technique, with white light, allows for the observation of the vortices. (b) Velocity profiles along the vorticity axis for $\dot{\gamma}$ =30, 40, 50 s^{-1}. The velocity is encoded as a grey level between 0 and $v_w(\dot{\gamma})$. (c) Time averaged velocity profiles $v_x(y)$ at a given location z for various shear rates. (d) Proportion of the high shear rate band as a function of $\dot{\gamma}$ measured from the optical or USV protocols. (e) Slip velocity at the inner cylinder as a function of $\dot{\gamma}$. (f) Local shear rate in the high shear rate band ($\dot{\gamma}_h$) as a function of $\dot{\gamma}$. (g) Local shear rate in the low shear rate band ($\dot{\gamma}_l$) as a function of $\dot{\gamma}$.

per were obtained for start-up flows at a known imposed shear rate. Typically, each start-up test was performed for ten minutes. In between each start-up flow experiment, the sample was allowed to relax and rest without flow for two minutes. Note nonetheless that most results presented in the paper have also been duplicated using start-up flows at imposed shear stress (*i.e.* creep tests). Except for the particulars of the early time transient response, the same behaviors were observed.

II. THREE CATEGORIES OF SHEAR-BANDING FLOWS

A. Background on elastic instabilities

It is well known that Newtonian fluids can exhibit increasingly unstable flows for large values of the Reynolds number $Re = \tau_{vd}\dot{\gamma}$, which gives the relative importance of destabilizing inertial forces and viscous stabilization—$\tau_{vd} \equiv \frac{d^2}{\nu}$ being the viscous diffusion time [59].

As mentioned in section I 4, in non-Newtonian fluids, the primary nonlinearity usually comes from the constitutive relation rather than from the momentum balance. The dimensionless group linked to the magnitude of nonlinear effects is the Weissenberg number $Wi \equiv \tau\dot{\gamma}$. For solutions of wormlike micelles, it had been long known that $Wi \sim 1$ was a rough estimate of the onset of shear-banding (if the corresponding value of the dimensionless stress was not higher than $\sigma_{xy}/G_0 \sim 1$) [4]. In short, shear-banding was known to be linked to Wi. With our recent experiments [37–40], we have also shown that, concomitantly, the Weissenberg number is also linked to the magnitude of destabilizing elastic forces that can lead to the emergence of secondary flows and eventually to 'elastic turbulence', a fact well known already for the–homogeneous–flows of polymer solutions [55–58].

In a 1990 seminal study, Larson, Shaqfeh and Muller showed in particular that the TC flow of polymer solutions could become unstable to a Taylor-like instability [55]. The kinematics of the unsteady flow are roughly similar to those of the Newtonian case, *i.e.* after a critical
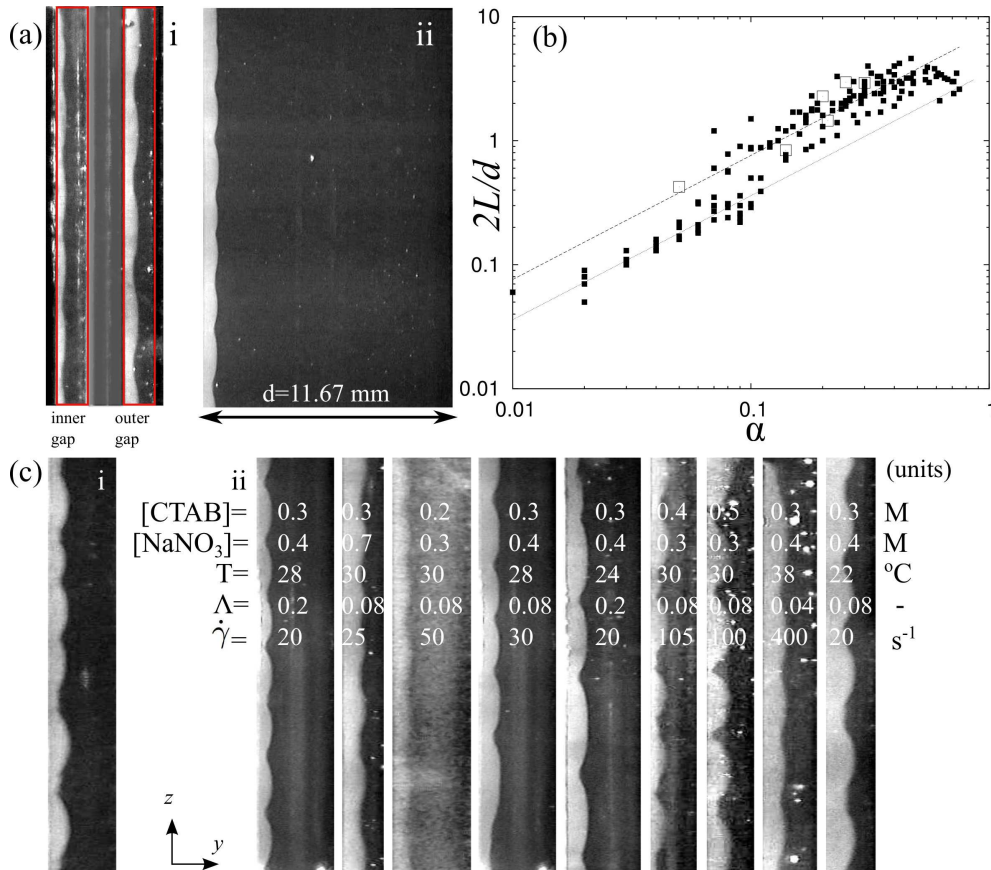
FIG. 4: (a)-i: Visualization of the inner and outer gaps in a cylindrical double-gap geometry. The fluid is [CTAB]=0.3 M and [NaNO$_3$]=0.4 M at T=30°C. The shear rates in the inner and outer gaps are respectively $\dot{\gamma}_{in} \simeq 35$ s^{-1} and $\dot{\gamma}_{out} \simeq 45$ s^{-1}. Both gaps are 1.5 mm wide, the inner gap with $\Lambda_i = 0.16$ and the outer gap with $\Lambda = 0.12$ (see ESI for details on the geometry). ii: [CTAB]=0.3 M and [NaNO$_3$]=0.4 M at T=30°C, in the cell with $\Lambda = 0.9$, for $\dot{\gamma} = 15$ s^{-1}. The horizontal and vertical scales are the same. (b) Summary across conditions ([CTAB], [NANO$_3$], T, Λ) of the dimensionless wavelength of the oscillations of the interface between bands $2L/d$ as a function of the proportion of the high shear rate band α. The white symbols are re-plotted from the (original 'OS') system of 10 wt % cetylpyridinium chloride in NaCl brine at T=21.5°C investigated in ref. [39]. The dashed line is the best fit of the data for [CTAB]=0.3 M and [NaNO$_3$]=0.4 M at T=28°C, the system previously discussed in ref. [40]. The equation for the lines is $\frac{2L}{d} = 2n\alpha$, with $n = 3.8$ for Λ=0.08 (dashed line) and n=2 for Λ=0.9 (dotted line). (c) Similar vorticity structuring of the secondary flows as observed by the oscillations of the interface between the bands of various systems. i: the system of 10 wt % cetylpyridinium chloride in NaCl brine at T=21.5°C for $\dot{\gamma} = 5$ s^{-1} investigated in ref. [39]. ii: many conditions for the CTAB/NaNO$_3$ system. The horizontal scale (given by the gap) is stretched twice in comparison to the vertical scale. All the data in (a-c) correspond to systems in C_2, or in C_3 before the onset of turbulent bursts (*cf.* section II E).

threshold, Taylor vortices appear, but the destabilizing mechanisms is linked to Wi rather than Re. Note that for both inertial and elastic mechanisms, if the geometry of the base flow is curved, the appropriate dimensionless group controlling the threshold to instability needs to take into account the curvature of the streamlines. In the simplest TC flow, where only the inner cylinder is rotating, and in the small gap limit, *i.e.* $d \ll R_i$, there exist two important dimensionless groups. The first one is relevant to the 'purely inertial TC instability':

$$\Sigma_i \equiv \sqrt{\Lambda} Re \qquad (1)$$

derived and observed by Taylor [60]. The second one is relevant to the 'purely elastic TC instability':

$$\Sigma_e \equiv \sqrt{\Lambda} Wi \qquad (2)$$

derived and observed by Larson *et al.* [55] when $Re \sim 0$. Here, $\Lambda \equiv \frac{d}{R_i}$ is the geometrical ratio linked to the streamline curvature. Note that the Taylor number is usually defined as $Ta \equiv \Sigma_i^2$ [59]. In the purely inertial case, the flow becomes unstable for $\Sigma_i > m'$. In the purely elastic case, the flow becomes unstable for $\Sigma_e > m$. Both m' and m are coefficients of order unity, with precise values that depend on the boundary conditions [59, 61].

B. Instability criterion for shear-banding flows

If one wishes to derive the appropriate dimensionless group for a purely elastic instability in the case of a shear-banding base flow, the key is to realize that the instability comes from the high shear rate band only, contrary to the flow of polymer solutions, which is homogeneous and where the entire sample becomes unstable. In small gap TC flow, the purely elastic dimensionless group is $\Sigma_e \equiv \sqrt{\Lambda} Wi$ for homogeneous flows. For shear-banded flows, it should be given by the following equation:

$$\Sigma \equiv \sqrt{\alpha \Lambda} Wi_h \qquad (3)$$

The gap d has been replaced by the 'effective gap', i.e. the band of high shear rate with width αd [40]. And the global Weissenberg number Wi has been replaced by the local Weissenberg number in the induced band $Wi_h \equiv \lambda \dot{\gamma}_h$ [40]. It is important to remember that the dimensionless group Σ should be the correct scaling for the instability of shear-banded base flows only if: (1) inertial effects are negligible, i.e. if the elasticity number $\mathcal{E}$ follows $\mathcal{E} \equiv Wi/Re \gg 1$, with Wi and Re taken in the appropriate domain; (2) for small gaps, i.e. $\Lambda \ll 1$; and (3) when there is no end effects $\Gamma \ll 1$.
For most of the experiments presented in this article, those three conditions will indeed be satisfied. The three TC cells with $\Lambda \simeq 0.04, 0.08, 0.2$ ($\Gamma \simeq 0.025, 0.025, 0.06$) satisfy the conditions $\Lambda \ll 1$ and $\Gamma \ll 1$. We will see in section III B that the TC cell with $\Lambda \simeq 0.9$ ($\Gamma \simeq 0.3$) does show behaviors departing from the small gap/no end effects approximation.

C. Irrelevance of inertial effects

To check if inertial effects are negligible in the high shear rate band, one must compute the elasticity number $\mathcal{E}_h$ associated with the different conditions investigated. We recall that in an unstable domain of width d, the Reynolds number is given by $Re = \tau_{vd} \dot{\gamma}$. In the case of shear-banded base flows, one must substitute $\dot{\gamma}$ by $\dot{\gamma}_h$. The viscous dissipation time to consider should also take into account the effective gap αd, and the viscosity of the high shear rate band. An order of magnitude for this local viscosity is the ratio $\eta_h \equiv \sigma_p/\dot{\gamma}_h$. Thus the elasticity number associated with the high shear rate band is given by:

$$\mathcal{E}_h = Wi_h \frac{\sigma_p}{\rho(\dot{\gamma}_h \alpha d)^2} \qquad (4)$$

where $\rho \simeq 10^3$ kg/m^3 is the density of the fluid. In our experiments, the lowest values of $\mathcal{E}_h$ correspond to solutions with a low concentration of surfactant, which have high values of $\dot{\gamma}_h$. For instance, for a band of a few millimeters wide, the solution of [CTAB]=0.2 M, [NaNO$_3$]=0.4 M at T=30°C has $\mathcal{E}_h \simeq 0.9 Wi_h$. Since in this case $Wi_h \simeq 10$, we have $\mathcal{E}_h \simeq 10 > 1$. It is large enough that elasticity

dominates, even if some 'inertio-elastic' effects may be detectable [62]. In most of the other conditions, we have $\mathcal{E}_h \gg 1$ and inertia has no effect.

This point is supported by experiments performed in a cylindrical double-gap geometry where the inner gap is in a TC configuration with the outer cylinder rotating while the outer gap is in a TC configuration with the inner cylinder rotating. It is well known that the inertial Taylor instability does not occur if only the outer cylinder is rotating [59, 60]. In contrast, in the purely elastic analogue, the instability does not depend on which cylinder is rotating [55]. Fig. 4a-i shows the secondary flow structure of a solution of [CTAB]=0.3 M, [NaNO$_3$]=0.4 M at T=30°C in this particular flow geometry. For this solution at the angular velocity of the inner hollow cylinder chosen here, the order of magnitude of the elasticity number in the high shear rate band is $\mathcal{E}_h \simeq 400$. Inertial effects are then supposed to be negligible. The fact that the structures of the secondary flow and thus of the oscillations of the interface are similar in both the inner and outer cylinder rotating situations unambiguously demonstrates the irrelevance of inertia. The slight difference on the wavelength is only due to the slight difference in α, because the inner and outer gaps support slightly different shear rates. The spatio-temporal dynamics of the two gaps are the same (see ESI). Note by the way that the (turbid) high shear rate band is localized at the inner wall of both the inner and outer gaps. It is because the high shear rate band is located in the region having the highest curvature [48–50] , where the shear stress is largest, independently of which cylinder is rotating.

D. Effective gap

The fact that in the formula for Σ (eq. 3), αd replaces d is well illustrated by the scaling of the characteristic dimension of secondary flows along the vorticity axis. In a Taylor-like vortex flow, the size of a pair of vortices $2L$– or equivalently, the size of a wavelength of the interface– scales with the size of the unstable domain in which it is contained. For instance, in the inertial case ($\mathcal{E} = 0$), if the cylinders are counter-rotating, the gap of the TC cell is split in two domains, one unstable near the inner cylinder and one stable near the outer cylinder [60, 63, 64]. Indeed, in the lab frame, there is a surface of zero velocity somewhere inside the gap, so for the outer domain the situation is equivalent to the situation of an outer cylinder rotating and an inner cylinder fixed. The original experiments of G.I. Taylor clearly showed that already [60]. Fig. 13-20 of Taylor's article showed secondary flows for counter-rotation, with vortices localized in the inner domain, shrinking with increasing outer rotation speed.

In the case of shear-banding base flows prone to elastic instability, the inner high shear rate band is the analogue of the inner domain in an inertial situation with contra-rotation. Instead of d we must consider the size of the band, i.e. αd. Fig. 4c-ii shows pictures of the plane

(y, z) for a representative set of tested systems of various [CTAB], [NaNO$_3$], T and Λ; at various imposed global shear rates $\dot{\gamma}$. All pictures were taken a few minutes after the beginning of the start-up test so that they are representative of the asymptotic flow. In all cases, we can see that the wavelength of the interface scales with the size of the high shear rate band. Fig. 4b gives the dimensionless wavelength of a pair of vortices as a function of the proportion of the high shear rate band α, for over 250 conditions ([CTAB], [NaNO$_3$], T, Λ, $\dot{\gamma}$). They all confirmed the following scaling:

$$\frac{2L}{d} = 2n\alpha \tag{5}$$

We have also reproduced the data from our previous study on the CPCl/NaSal system [39]. They overlap well, showing *a fortiori* no difference between different surfactants. The picture of the CPCl/NaSal system in Fig. 4c-i is essentially indistinct from pictures of the CTAB/NaNO$_3$ system.

In ref. [40] we fitted the data for a system of [CTAB]=0.3 M and [NaNO$_3$]=0.4 M at T=28°C in a TC cell with $\Lambda \simeq 0.08$. We found $n = 3.8 \pm 0.1$. This fit is reproduced here by the straight dashed line. It seems to fit all the data gathered on the various solutions reasonably well.

Note that the data at low α come from experiments done on the TC cell with $\Lambda \simeq 0.9$ ($\Gamma \simeq 0.3$). Fig. 4a-ii shows an example of shear-banding flow in this TC cell. The data for this TC cell also follow a linear scaling but with a lower value of n ($n \simeq 2$). This may be due to behaviors departing from the small gap/no end effects approximation, as discussed in section III B.

Note also that for $\alpha \gtrsim 0.6$ the wavelength usually levels off or even decreases slightly. This is due to the onset of a particular spatiotemporal dynamics of the vortex flow [36, 40].

E. Three categories of shear-banding

Let us now recall the implications of the instability criterion (Eq. 3) that we derived in Ref. [40]. We have seen in section I 5 that the local Weissenberg number Wi_h in the high shear rate band depends on the global Weissenberg number Wi, due to slip at the moving wall. However, velocimetry data also show that, for large enough bands (typically for $\alpha > 0.3$) and provided that the shear-banding flow does not become turbulent, Wi_h is of the same order as the upper boundary of the stress plateau $Wi_h \simeq Wi_h^*$. Since Wi_h^* increases with the surfactant concentration and decreases with temperature (section I 4), concentrated/low temperature solutions should be more prone to instability in a given TC cell.

We can actually make a finer prediction. Let us recall that we expect a shear-banded base flow to become unstable if $\Sigma > m$, where m is a coefficient of order unity, whose precise value depends on the boundary
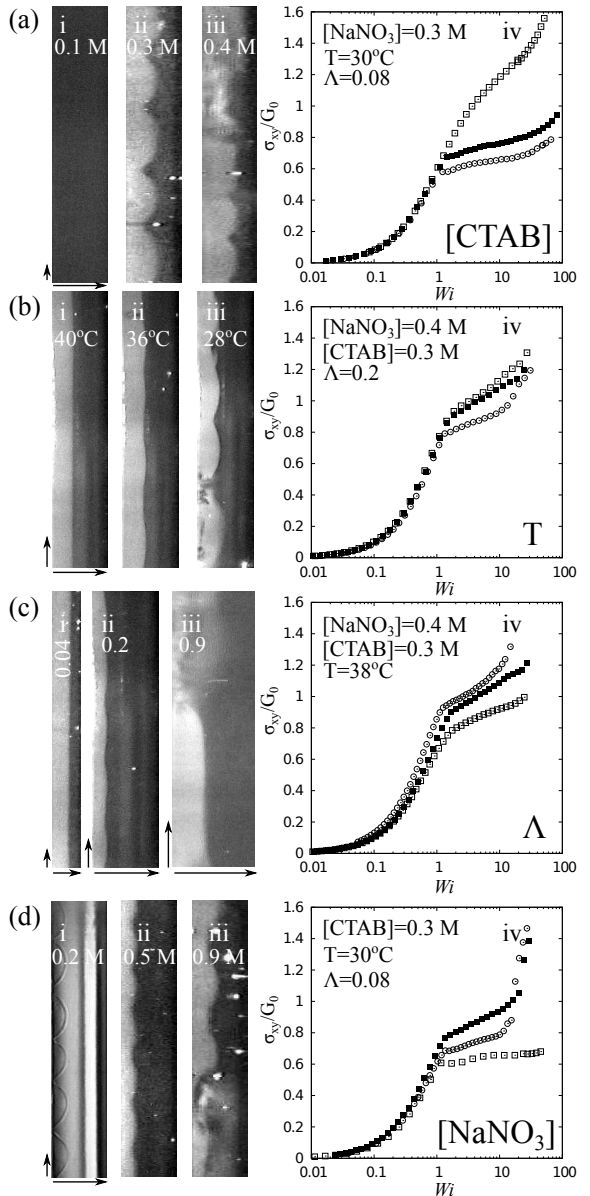

FIG. 5: Categories of shear-banding for varying surfactant concentration [CTAB] (a), temperature T (b), geometry Λ (c), and salt concentration [NaNO$_3$] (d). On each sub-figure, (i-iii) are pictures of the gap (y, z) and (iv) shows the dimensionless flow curves corresponding to i ($\square$), ii ($\blacksquare$) and iii ($\circ$). The parameters held constant are given in (iv), while the value of the varying parameter is given directly on (i-iii). The arrows on the bottom left corner of each picture give the relative scales of the y and z axes. All images represent the entire width of the gap, except for c-iii that only shows $d/4$. (a-d)-iii represent snapshots of turbulent bursts, thus for fluid in C_3. (a-d)-ii represent snapshots of vortex flows regularly deforming the interface between bands. For those systems, $\alpha = 1$ is reached without the occurrence of turbulence and for $Wi \in [Wi_h^*, Wi_c]$ the flow is homogeneous and secondary flows disappear. The fluids are in C_2. (b,c)-i represent snapshots of stable shear-banding flows, with a flat interface between bands, thus in C_1. In (a)-i, the shear-banding base flow disappears before we can reach C_1. In (d)-i, the low concentration of salt prevent us from observing the turbidity contrast between bands. But bands can be imaged with white light, revealing that even for [NaNO$_3$]=0.2 M, we are still in C_2 (see section III for more informations on the effect of salt).

conditions [59, 61]. The structure of the secondary flows may also depend on the boundary conditions.

At the end of the shear-banding regime, *i.e.* when $\alpha = 1$, the boundary conditions on the unstable domain are modified. As long as $\alpha < 1$ the interface with the low shear rate band acts as a soft boundary, then when $\alpha = 1$, the soft interface vanishes and is replaced by a hard wall.

We can define m_s and m_h to be the values of m corresponding respectively to 'soft' and 'hard' boundary conditions. Because $m_s < m_h$ [40, 61], we can use basic Boolean logic to classify shear-banding flows into three possible categories depending only on the values of Λ and Wi_h:

- *Category 1* (C_1)

For sufficiently low Wi_h–*i.e.* high T, low Λ and low concentration–the shear-banding flow is stable for any α, since $\Sigma < m_s$ even for $\alpha = 1$. The flow can then become unstable for Weissenberg numbers above a critical value $Wi_c > Wi_h$ as in the case of a regular viscoelastic fluid, *i.e.* following the scaling $\Sigma_e = \sqrt{\Lambda} Wi$.

- *Category 2* (C_2)

For intermediate values of Wi_h–*i.e.* intermediate T, Λ and concentration–the shear-banding flow is unstable above a critical value α_c when $\Sigma > m_s$ for $\alpha > \alpha_c$. Then as the imposed shear rate is increased and $\alpha \to 1$ the boundary conditions change and the flow is stabilized, because the flow is below the threshold m_h. Eventually for $Wi > Wi_c > Wi_h$ the flow becomes unstable again.

- *Category 3* (C_3)

Finally, if Wi_h is high enough–*i.e.* for low T, high Λ and high concentration–we have two critical band widths α_{c1} and α_{c2}. For $\alpha > \alpha_{c1}$, $\Sigma > m_s$. And for $\alpha > \alpha_{c2}$, $\Sigma > m_h$. In this case, there is no stabilization for $Wi > Wi_h$. The flow remains unstable, although the spatiotemporal characteristics may change.

Note that if one is interested in the stability of the low shear rate band, $\dot{\gamma}_l$ and $[1 - \alpha]d$ must be used to compute the relevant stability criterion. Low shear rate bands prone to elastic instability could compromise the onset of shear-banding. This could be a category C_4, but we found no evidence for it in all conditions tested. The Weissenberg number in the low shear rate band is always low.

Overall, if concentrations of surfactant and salt, temperature and the shearing geometry are allowed to vary, we expect changes in the stability of shear-banding flows. Concentrations and temperature modify Σ through the value of Wi_h. The geometry of the TC cell modifies Σ through Λ. Any way of increasing Σ should result in similar changes in the category of shear-banding flow: from C_1 to C_2 and eventually to C_3 as Σ increases.

In previous studies we found first evidence for C_2 [38] and C_3 [39] by using two different systems with fixed thermodynamical and geometrical conditions [CTAB (0.3 M)/NaNO$_3$ (0.405 M) at $T = 28°$C and CPCl/NaSal 10% in NaCl brine at $T = 21.5°$C]. Here, using large ranges of values for the different parameters ([CTAB], [NaNO$_3$], T, Λ, $\dot{\gamma}$), we demonstrate the relevance of the criterion in most of the tested conditions.

1. *Effect of [CTAB]*

Fig. 5a illustrates the effect of increasing surfactant concentration on the type of secondary flows. Those experiments have been conducted in a TC cell with $\Lambda = 0.08$, at $T = 30°$C in solutions with [NaNO$_3$]=0.3 M and varying surfactant concentrations [CTAB]. For [CTAB]$\geq$ 0.4 M shear-banding flows are clearly in C_3. Indeed, before the end of the shear banding regime, *i.e.* before $\alpha = 1$, we observe the onset of turbulent bursts similar to the one described in detail in ref. [39]. The turbulent bursts destabilize the 3D shear-banded vortex flow and the system undergoes a transition towards elastic turbulence before reaching the *true* end of the plateau, *i.e.* before $\alpha = 1$. For [CTAB]=0.3 and 0.2 M, the shear-banding flows is in C_2 while for [CTAB]=0.1 M, the shear-banding flow disappeared altogether. Therefore, in this last case, we could not observe C_1.

2. *Effect of T*

Fig. 5.b displays the effect of increasing temperature on the type of secondary flows. Those experiments have been conducted in a TC cell with $\Lambda = 0.2$, in solutions with [CTAB]=0.3 M and [NaNO$_3$]=0.4 M, and varying temperature T. For $T \leq 34°$C shear-banding flows correspond to the C_3 category, since turbulent bursts, clearly localized in the high shear rate band, develop before the end of the shear-banding regime. For $34 < T \leq 40°$C, the shear-banding flows are in C_2. Finally, for $T \geq 40°$C, the shear-banding flows are in C_1. Note that we have also conducted experiments with varying temperatures on the same surfactant system in TC cells with $\Lambda = 0.04$, 0.08 and 0.9. In the cells with $\Lambda = 0.04$ and 0.08, C_3 could not be reached, because even at $T = 22°$C, Σ is still too small. Finally, temperatures below $T = 22°$C cannot be reached because the surfactant demixes. For $\Lambda = 0.9$, it is the opposite, C_1 could not be reached, even at $T = 40°$C. We refrained from going to higher temperature because of the sensitivity of our home made TC device. In the ESI we show the disappearance of secondary flows as the boundary between C_2 and C_1 is crossed for a system under a constant shear rate but with quasi-static increase of the temperature.

3. *Effect of Λ*

In Fig. 5c, we show the effect of increasing the curvature of the base flow streamlines Λ on the type of sec-

ondary flows. Those experiments were conducted with solutions of [CTAB]=0.3 M and [NaNO$_3$]=0.4 M, at $T = 38°C$, and for varying Λ. For $\Lambda = 0.9$ shear-banding flows are in C_3. Here again, the dynamics of turbulent bursts is similar to the ones in ref. [39]. In such a large gap, turbulence is unmistakeably localized in the high shear rate band. Fig. 5c-iii gives a snapshot showing only the quarter of the gap close to the inner cylinder. The low shear rate band in the three other quarters of the gap is completely unaffected by the turbulence in the high shear rate band. For $\Lambda = 0.2$ the shear-banding flows are in C_2. Finally, for $\Lambda = 0.08$ and 0.04, they are in C_1. Note that we have also changed Λ at other temperatures and we have observed the same phenomenology. Note however that the TC cell with $\Lambda = 0.9$ goes beyond the small gap/small aspect ratio. We will discuss this in section III B.

4. Effect of [NaNO$_3$]

Fig. 5d displays the effect of varying the salt concentration [NaNO$_3$] on the type of secondary flows. As discussed in section I 4, the effect of salt on Wi_h^* are more subtle and the three categories are not observed in a simple order. For the results in the figure, we only increased salt concentration up to the maximum of λ around [NaNO$_3$]$\simeq$ 1 M (*cf.* Fig. 1c). For higher salt concentrations, other effects come into play, as discussed in section III C. The experiments have been conducted with solutions of [CTAB]=0.3 M at $T = 30°C$, in a TC cell with $\Lambda = 0.08$. For [NaNO$_3$]$\geq$ 0.7 M, shear-banding flows are in C_3 and turbulent bursts occur. For [NaNO$_3$]= 0.5 and 0.6 M, the shear-banding flows are in C_2 and the turbidity contrast between bands is standard. But, even for [NaNO$_3$]=0.2 M, we cannot not reach C_1. Note moreover that at low concentrations in salt, the turbidity contrast between the bands becomes too low and the band structure needs to be imaged using white light [37].

5. Impact on dimensionless flow curves

Fig. 5a,b,c,d-iv give the dimensionless flow curves for the three examples of flows given in Fig. 5a,b,c,d-i to iii. It seems that Wi_h^* increases with the surfactant concentration, justifying the increase of Σ responsible for the changes in categories of shear-banding. Note nonetheless that since the system with [CTAB]= 0.4 M is in C_3, Wi_h^* is smaller than the true end of the plateau. A similar phenomenology is observed for changes in the temperature.
Changes in Λ illustrate once more the importance of secondary flows on the apparent flow curves as already mentioned in section I 2 (*cf.* Fig. 2b).
Finally, changes in salt concentration have a subtler effect as mentioned already in section I 4. In Fig. 5d-iv, the flow curve for [NaNO$_3$]=0.5 M has a higher dimen-

sionless plateau and thus a lower expected value of Wi_h^* than the flow curve for [NaNO$_3$]=0.9 M. But for lower concentrations of salt, in particular [NaNO$_3$]=0.2 M, σ_p/G_0 seems to decrease and Wi_h^* seems to increase. The disappearance of the turbidity contrast between bands suggests a change in mesoscopic structure that may be responsible for this non-monotonicity in the behaviors of σ_p/G_0 and Wi_h^* *vs* [NaNO$_3$].

F. Spatiotemporal dynamics of the secondary flows

The theoretical framework developed in ref. [40] and recalled in section II E should give us the onset of secondary flows when $\Sigma > m$. But this criterion does not give us any information on the precise spatiotemporal dynamics of the vortex flows.

For the inertial TC problem, it is well known that a variety of spatiotemporal patterns can be observed [65, 66]. When only the inner cylinder is rotating, the vortex flow is first steady (*Taylor vortex flow* or *TVF*). As Σ_i is increased further, the vortex flow becomes wavy (*wavy vortex flow* or *WVF*), then *modulated waves* develop and, eventually, a regime of *turbulent Taylor vortices* is reached.

For the purely elastic TC problem, the situation is not yet fully sorted out. Linear stability analysis found that the first unstable modes are non-axisymmetric and oscillatory [67]. But the first experiments seemed to suggest otherwise [68–70]. Baumert and Muller found steady axisymmetric modes with a very long onset time. A potential explanation for the discrepancies has since emerged [62]. The explanation involves thermal effects. Indeed, the viscosity of the fluids used in experiments being high, viscous heating can produce temperature gradients that in turn result in gradients in fluid viscosity and fluid elasticity. The axisymmetric modes found by Baumert and Muller are now understood to be 'thermo-elastic' modes [71, 72]. In isothermal conditions, the typical flow pattern is indeed non-axisymmetric and time dependent. It is the so-called flame pattern [69–71], which can also be observed when inertia and elasticity both play a role [62]. The flame pattern is constituted of 'di-whirls' [73–79]. The diwhirls are mostly solitary vortex pairs with a very strong and localized inward flow and a very broad and weak outward flow. Diwhirls can be created spontaneously in regions of outflows (see Fig. 26 of ref. [69] and Fig. 10 of ref. [70]) and they can merge when they come too close to each other. When they merge, it is always the counter-rotating vortices separated by an outflow that annihilate each other [73, 74]. It has been argued that this particular type of structure is characteristic of secondary flows driven by elasticity.

For shear-banding surfactant solutions, our previous studies have identified several important features of the spatiotemporal dynamics of secondary flows. For small widths of the high shear rate band ($\alpha \lesssim 0.1$), the vor-
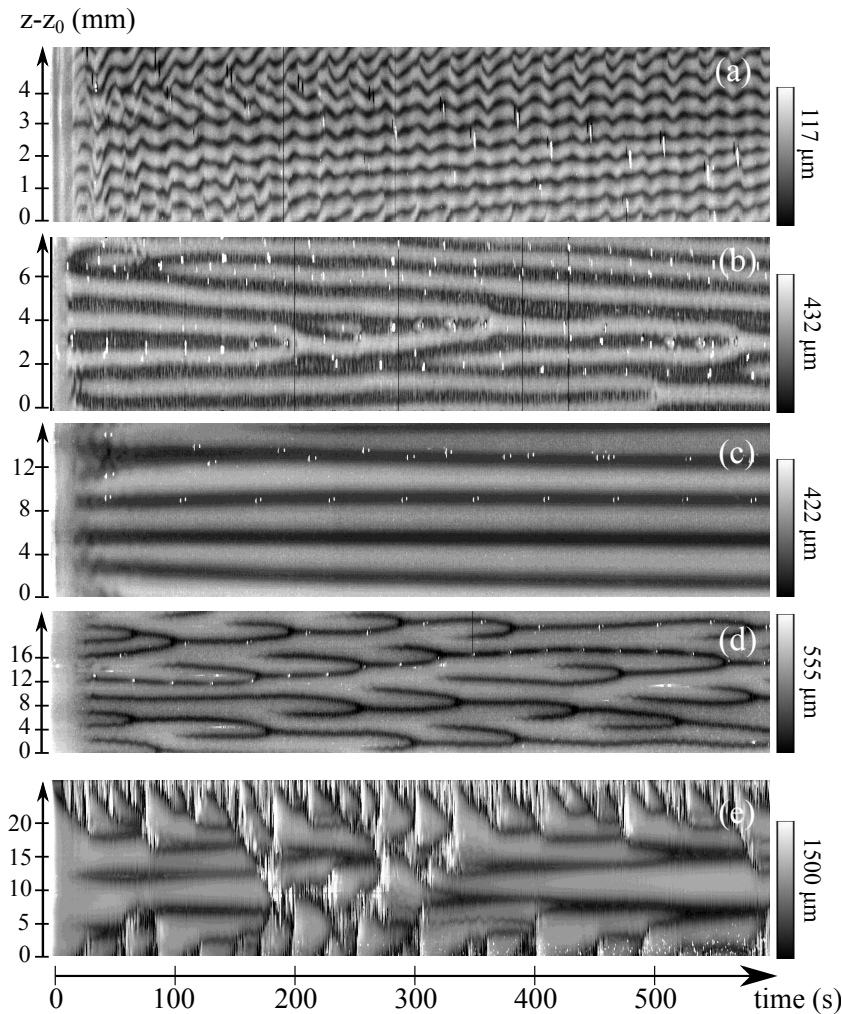
z-z$_0$ (mm)

FIG. 6: Example of the classes of spatiotemporal dynamics of secondary flows inferred from the evolution of the position of the interface between band during a step shear rate from rest. (a) *Zig-zag* pattern for [CTAB]=0.3 M, [NaNO$_3$]=0.4 M, T=28°C, $\Lambda = 0.04$ and $\dot\gamma = 10$ s^{-1}; (b) *Anti-flame* pattern for [CTAB]=0.4 M, [NaNO$_3$]=0.3 M, T=30°C, $\Lambda = 0.08$ and $\dot\gamma = 40$ s^{-1}; (c) *Steady vortex flow* pattern for [CTAB]=0.3 M, [NaNO$_3$]=0.5 M, T=30°C, $\Lambda = 0.08$ and $\dot\gamma = 50$ s^{-1}; (d) *Flame* pattern for [CTAB]=0.3 M, [NaNO$_3$]=0.3 M, T=30°C, $\Lambda = 0.08$ and $\dot\gamma = 250$ s^{-1}; (e) *Turbulent burst* pattern for [CTAB]=0.3 M, [NaNO$_3$]=0.4 M, T=28°C, $\Lambda = 0.2$ and $\dot\gamma = 50$ s^{-1}. The amplitude of the interface oscillations is given in grey scale. The vertical axis represents the spatial coordinate along the cylinder axis with an origin z_0 taken roughly at the middle of the TC cell ($z_0 \simeq 20$ mm from the bottom of the cell). Periodic white dots on some patterns are due to small bubbles trapped in the flow during the loading of the sample or by an instability of the free surface near the axis of the inner cylinder.

tex flow was oscillating along the vorticity direction in a characteristic *zig-zag* pattern [35, 36, 39]. For intermediate widths, the vortex flow was steady, with the boundaries of the vortices oscillating slightly with a period of a few times the relaxation time λ [36, 37]. For the largest widths ($\alpha \gtrsim 0.6$) pair of vortices could be created and annihilated in a way reminiscent of the *flame* pattern [35–37]. In the CPCl/NaSal 10% system, the flame pattern could not be reached because of the onset of *turbulent bursts*, disturbing the band structure more and more frequently as the global shear rate increased [39].

In the present study, we have greatly increased the range of systems investigated but found the same succes-

sion of spatiotemporal patterns, except for the discovery of a new intriguing one. First, for small proportions, the vortex flows follow a *zig-zag* pattern. As an example, Fig. 6a shows the zig-zag pattern observed for a solution of [CTAB]=0.3 M and [NaNO$_3$]=0.4 M at T=28°C in a TC cell with $\Lambda = 0.04$ for $\dot\gamma = 10$ s^{-1}. Previously, we had noticed that the zig-zag and steady vortex flow patterns were separated by a small crossover where we could observe an asymptotic wavelength of the pattern half of the initially growing wavelength (Fig. 11f of ref [36]). By studying the spatiotemporal dynamics on a wider range of conditions than before, we have found that this crossover region actually corresponded

to a pattern in itself: the *anti-flame* pattern. Fig. 6b gives an example of the anti-flame pattern for a solution of [CTAB]=0.4 M and [NaNO$_3$]=0.3 M at T=30°C in a TC cell with $\Lambda = 0.08$ for $\dot\gamma = 40$ s^{-1}. We call it 'anti-flame' because pairs of vortices can be created in regions of inflow and they can merge but always by the annihilation of counter-rotating vortices separated by an inflow, shaking some of the arguments made on diwhirls [73–79]. The anti-flame pattern is followed by a *steady vortex flow*. Most of the time, a time variation can be seen, but we cannot analyse it in enough details to confirm that this time periodicity is always of the scale of λ. In some cases, the time periodicity is not even detectable, as in the example given in Fig. 6c. Finally, we have been able to reach a *flame* pattern (Fig. 6.d) for a solution of [CTAB]=0.3 M and [NaNO$_3$]=0.3 M at T=30°C in a TC cell with $\Lambda = 0.08$ for $\dot\gamma = 250$ s^{-1}.

Note that it is still unclear what is the control parameter for the transitions between spatiotemporal dynamics. We always observe the succession from zig-zag, to anti-flame, to steady vortex flow, to flame for increasing α, but it is unclear if the transition thresholds scale with α, $\alpha\Lambda$, Σ or even something else. Experiments seem to discard a scaling on solely α. For instance, in the TC cell with $\Lambda = 0.2$, with the reference system of [CTAB]=0.3 M and [NaNO$_3$]=0.4 M at T=28°C, we observe a transition toward the flame pattern for values of αd similar to the one in the TC cell with $\Lambda = 0.08$ [36, 37], even though the corresponding values of α are widely different. A scaling on Σ would be hard to identify, because when Σ increases, systems tend to switch to C_3 where turbulence disturbs the spatiotemporal dynamics of the vortices (*cf.* Fig. 6e).

It is important to remember that the succession of patterns is only seen if the vortex flows are unperturbed by turbulent bursts. When a system is in C_3, turbulence bursts become more and more frequent as the global shear rate is increased. In ref. [39], the turbulent bursts occurred too frequently before we could see the flame pattern. But in Fig. 6e, we give an example of turbulent bursts occurring on top of a flame pattern, in a solution of [CTAB]=0.3 M and [NaNO$_3$]=0.4 M at T=28°C in a TC cell with $\Lambda = 0.2$ for $\dot\gamma = 50$ s^{-1}.

III. DISCUSSION: BEYOND THE PURELY ELASTIC INSTABILITY SCALING

In this article, we have demonstrated that the emergence of secondary flows in solutions of wormlike micelles can be well interpreted by a purely elastic instability of the high shear rate band. This purely elastic instability is similar to the one observed in polymer solutions. The only difference concerns the base flow. In polymer solutions, the base flow is homogeneous. In wormlike micelles solutions, the base flow is shear-banded. The deformation of the interface between bands follows from the onset of secondary flows localized in the high shear rate band.

And the prediction of three categories of shear-banding is a consequence of the switch in boundary conditions when $\alpha \to 1$.

Overall, both the homogeneous case Σ_e (eq. 2) and the shear-banded case Σ (eq. 3) are instances of the same underlying 'purely elastic instability scaling':

$$\Sigma_{\mathcal{D}} \equiv \sqrt{\Lambda_{\mathcal{D}}}Wi_{\mathcal{D}} \Rightarrow \begin{cases} \text{if } \alpha = 1, \ \Sigma_{\mathcal{D}} = \Sigma_e \\ \text{if } \alpha \neq 1, \ \Sigma_{\mathcal{D}} = \Sigma \end{cases} \quad (6)$$

where $\Lambda_{\mathcal{D}}$ and $Wi_{\mathcal{D}}$ need to be taken in the appropriate unstable domain $\mathcal{D}$. The parameter α is just an indicator of the type of base flow. This is actually a consequence of the general scaling for any flow with curved streamlines derived by Pakdel and McKinley [40, 57].

It is not necessarily always the case, however, that secondary flows in solutions of wormlike micelles can be well described by a scaling of the form $\Sigma_{\mathcal{D}}$. We have seen already that the scaling encompassed in Σ can be inaccurate if the system under investigation fails to respect: (1) the creep flow hypothesis ($\mathcal{E} \gg 1$); (2) the small gap hypothesis ($\Lambda \ll 1$); and (3) the large aspect ratio hypothesis ($\Gamma \ll 1$). Those three hypotheses limiting the validity of the scaling were explicitly needed by the theoretical framework used in ref. [40]. But actually, there are other implicit hypotheses. We could underline some of them from rational grounds, but most are suggested to us empirically. Experiments on a wide range of conditions sometimes lead us to explore extreme values of the parameter space ([CTAB],[NaNO$_3$], T, Λ, Γ, $\dot\gamma$) and we have clearly observed deviations from small gap and large aspect ratio (III B).

We have also found that the excess of salt could lead to modifications on the spatiotemporal dynamics of secondary flows (III C). We also realized that secondary flows could eventually disturb the structure of the bands, resulting in a feedback between the structure and the secondary flows (III D). Finally, we will come back on an important point that we have left unspoken: the potential effects of interfacial modes (III E).

Overall, if the criterion seems qualitatively valid, all the effects deviating from the purely elastic instability scaling severely limited our experiments to too small a range of systems to quantitatively check the scaling Σ given in eq. 3. We do not have at our disposal enough reliable systems to have a large range of $\alpha\Lambda$ and Wi_h to draw a stability diagram similar the one predicted in Fig. 3 of ref. [40]. Moreover, we refrained from computing more than orders of magnitude for Σ since we know that the apparent end of the shear-banding plateau Wi_h^* is not reliably equal to the local value Wi_h in the high shear rate band for a given global Wi (III A).

A. Systematic wall slip

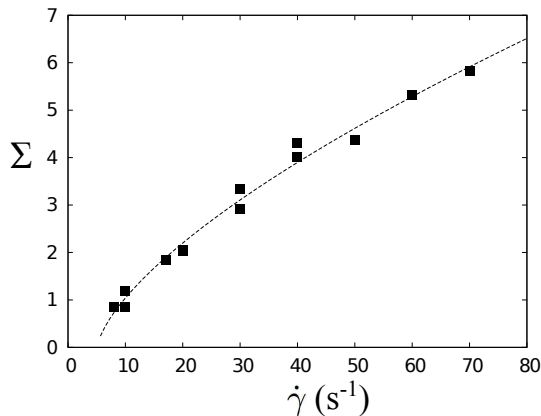Even when turbulence does not lead to an up-turn in the flow curve before the true end of the shear-banding

FIG. 7: Instability criterion $\Sigma = \sqrt{\alpha \Lambda} Wi_h$ computed as a function of the global shear rate $\dot{\gamma}$. The dashed line is the best fit for $\Sigma = a(\dot{\gamma} - \dot{\gamma}_l)^b$, with $\dot{\gamma}_l = 5 \pm 2$ s^{-1}, $a = 0.4 \pm 0.1$ s^b and $b = 0.67 \pm 0.06$.

regime ($\alpha = 1$), wall slip leads (at least at the beginning of the banding regime) to :

$$Wi_h^* \neq Wi_h \tag{7}$$

We chose to highlight this difference in an equation, because it has such an impact on the pragmatic use of the scaling Σ. If, following the simple lever rule, the local value of the Weissenberg number in the high shear rate band Wi_h is constant and equal to the end of the plateau on the flow curve Wi_h^*, then we can compute Σ easily. But we have shown in Fig. 3 that wall slip leads to a variation of the local Wi_h with the global Wi, with only rigorously $Wi_h = Wi_h^*$ when $\alpha = 1$ (assuming that the system is in C_2). Moreover, theoretical arguments suggest that wall slip is a necessary feature of shear-banded flows [12]. Wall slip and a variation of Wi_h with Wi seem to be required for the global shear rate in the gap to match the value imposed by the rheometer [12]. Such effects have been observed in many cases [17, 24, 32], and they seem to be a manifestation of non-local effects [12, 82, 83]

This wall slip does not violate the scaling Σ given in eq. 3, but it means that we cannot use Wi_h^* but should use the local Wi_h given by velocity measurements. Fig. 7 gives the computation of the value of $\Sigma(\dot{\gamma})$ based on velocity measurements to compute Wi_h, for the solution of [CTAB]=0.3 M and [NaNO$_3$]=0.4 M at T=28°C, in a TC cell with $\Lambda \simeq 0.08$. The dashed line is the best fit for $\Sigma = a(\dot{\gamma} - \dot{\gamma}_l)^b$, with $\dot{\gamma}_l = 5 \pm 2$ s^{-1} the critical shear rate for the onset of shear-banding and $a = 0.4 \pm 0.1$ s^b, $b = 0.67 \pm 0.06$. Note that if we had $Wi_h = Wi_h^*$ and a simple lever rule, we would have $\Sigma \sim \dot{\gamma}^{1/2}$, because $\alpha \sim \dot{\gamma}$. The fact that $b = 0.67 > \frac{1}{2}$ comes from the fact that $Wi_h \sim \dot{\gamma}^c$ with $c > 0$.

Note that this particular solution is in C_2 but that a slight increase of surfactant concentration, or a slight decrease in temperature would put it in C_3. Thus, this indicates that the value of Σ close to the beginning of
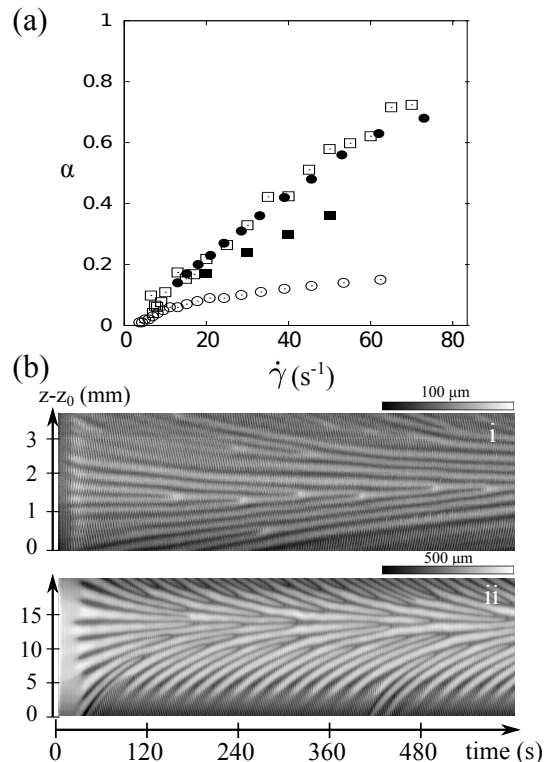

FIG. 8: (a) Proportion of the high shear rate band α as a function of the global shear rate $\dot{\gamma}$, imposed by the rheometer. The system is a solution of [CTAB]=0.3 M and [NaNO$_3$]=0.4 M at T=28°C, in TC cells with $\Lambda \simeq 0.04$ (●), $\Lambda \simeq 0.08$ (□), $\Lambda \simeq 0.2$ (■) and $\Lambda \simeq 0.9$ (○). (b) Spatiotemporal dynamics of vortex flows modified by small aspect ratio effects in the TC cell with $\Lambda = 0.9$: (i) Modified anti-flame for $\dot{\gamma} = 6$ s^{-1} and (ii) modified flame for $\dot{\gamma} = 10$ s^{-1}. The location z_0 at which the dynamics is recorded is such that the middle of the height of the pattern coincides with $H/2$.

the shear-banding regime (for $\dot{\gamma} \gtrsim \dot{\gamma}_l$) is greater than m_s, while the value of Σ at the end of the shear-banding regime (for $\dot{\gamma} = \dot{\gamma}_h$) is just under m_h. From Fig. 7 we conclude that $m_s \simeq 1$ and $m_h \simeq 7$.

B. Deviations from small gap and small aspect ratio

As mentioned in section II B, the TC cell with $\Lambda \simeq 0.9$ and $\Gamma \simeq 0.3$ does show behaviors departing from the small gap and no end effects approximations. First, the effect of large gap is that the global shear rate has a large inhomogeneity. For this reason, at the same imposed shear rate $\dot{\gamma}$, in TC cells with different Λ, the proportion of the high shear rate band is not the same. Fig. 8a shows how for TC cells with $\Lambda = 0.2$ and even more for $\Lambda = 0.9$, the deviation from the simple lever rule is unmistakable.

In the TC cell with $\Lambda = 0.9$, we also have $\Gamma = 0.3$, *i.e.* the gap height is just a bit more than three times its width. A striking consequence can be observed on the

15

spatiotemporal dynamics of the vortex flows. When the large aspect ratio holds ($\Gamma^{-1} \gg 1$), the spatiotemporal patterns, for instance in Fig. 6, are globally invariant along the vorticity axis z. They are periodic along z of course, but the top and bottom of the cell do not have a significant effect on the pattern. For $\Lambda = 0.08$, we have $\Gamma = 0.025$. If we only fill the gap half way up, $\Gamma' = 0.05$ still respects the large aspect ratio. In such conditions we can not see any significant impact on the spatiotemporal pattern (data not shown). In contrast, when $\Gamma = 0.3$ in the large gap cell, we observe clear influences of the top and bottom ends of the TC cell. For instance, for [CTAB]=0.3 M and [NaNO$_3$]=0.4 M at T=28°C, Fig. 8b gives a modified anti-flame pattern for $\dot{\gamma} = 6$ s^{-1} (i) and a modified flame pattern for $\dot{\gamma} = 10$ s^{-1} (ii). In both cases, the original large aspect ratio pattern is partly overlapped by travelling waves going from the top and bottom ends towards the center of the TC cell ($z = H/2$). Similar phenomenon occurs in the inertial TC instability with short aspect ratios [66]. Note that a fast zig-zag mode is also superimposed to the anti-flame pattern during the first four minutes.

Note that when Γ becomes large, the base flow between cylinders is not simply a purely annular Couette flow. In a Couette flow, surfaces of streamlines under the same stress have only one radius of curvature, linked to their radial position. In more general cases, including the case of TC flows with small aspect ratios, the occurrence of $\Lambda_{\mathcal{D}}$ in the instability scaling (eq. (6)) must be replaced by a combination of $\Lambda_{\mathcal{D}}$ and $\Gamma_{\mathcal{D}}$, where $\Gamma_{\mathcal{D}}$ is taken in the appropriate domain [57].

C. Effects of the salt concentration

As mentioned with respect to Fig. 1c, the salt concentration is known to have some effects on the mesoscopic architecture of networks of wormlike micelles. The mesoscopic architecture is modified even in the absence of flow as reflected by changes in the behavior of the viscoelastic parameters obtained in linear rheology. For concentrations up to [NaNO$_3$]$\simeq$ 1 M, the main effect of increasing salt concentration seems to be an increase in the average length of micelles. But we have seen in Fig. 5d that it also has some unexplained effect on the turbidity of high shear rate bands. For low concentrations of salts, [NaNO$_3$]$\leq$ 0.2 M, the turbidity contrast seems to disappear completely and the dimensionless flow curve has a lower plateau than for higher concentrations of salt. If the effect of salt is just to increase the length of worms as for an increase in surfactant concentration, we would expect the opposite behavior [4].

For [NaNO$_3$]$\geq$ 1 M, the relaxation time λ decreases with increasing salt concentration, as shown in Fig. 1c. This decrease supposedly reflects the effect of branching of micelles [5, 42]. The effect of such branching on the nonlinear rheology is still unsettled [5]. Our experiments on solutions of [CTAB]=0.3 M for salt concentrations
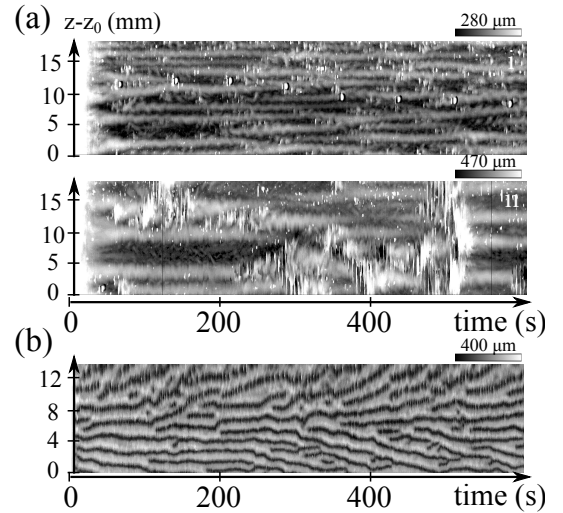

FIG. 9: Spatiotemporal dynamics of vortex flows for high concentrations of salt. (a) [CTAB]=0.3 M and [NaNO$_3$]=1.2 M at T=30°C, and $\Lambda = 0.08$. (i) $\dot{\gamma} = 20$ s^{-1}. (ii) $\dot{\gamma} = 30$ s^{-1}. (b) [CTAB]=0.3 M and [NaNO$_3$]=2.8 M at T=30°C and $\Lambda = 0.08$, $\dot{\gamma} = 300$ s^{-1}.

[NaNO$_3$]> 1 M can give a few interesting indications. First, even for very large salt concentrations, the turbidity contrast between bands is still strong. Then, the spatiotemporal dynamics of secondary flows can be altered by high concentrations of salt. We have noted two types of consequences illustrated on examples in Fig. 9a and b.

Figure 9a gives two spatiotemporal patterns observed for a solution of [CTAB]=0.3 M and [NaNO$_3$]=1.2 M at T=30°C, in the TC cell with $\Lambda = 0.08$. They are representative of the spatiotemporal dynamics for concentrations of salt not much higher than [NaNO$_3$]$\simeq$ 1 M. They resemble the spatiotemporal dynamics for the vortex flows described in section II F, except that they are disrupted by turbidity fluctuations. The patterns resemble those corresponding to situations where impurities are present in the sample, generating enhanced wall slip [39].

Fig. 9b gives the spatiotemporal dynamics of a solution of [CTAB]=0.3 M and [NaNO$_3$]=2.8 M at T=30°C, in the TC cell with $\Lambda = 0.08$. It is an example of the effects of even higher concentrations of salt. The spatiotemporal patterns are strongly altered and appear chaotic. The spatiotemporal pattern seems to be a combination of the flame and anti-flame patterns.

D. Feedback beetween the band structure and secondary flows

In the purely elastic instability scaling given in eq. 3, the formula includes αd, the width of the effective gap. Interestingly, if secondary flows are generated, they tend
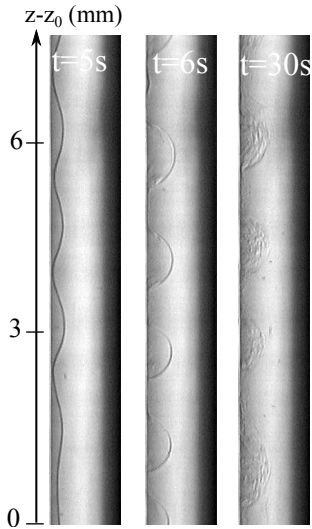
FIG. 10: Three snapshot of the gap of a solution of [CTAB]=0.55 M in D_2O (20 wt %) at T=37.5°C, in a TC cell with $\Lambda = 0.08$. The gap is illuminated by white light (the illumination is made non-homogenous in the gap in order to increase the contrast between the high and low shear bands). The three pictures are taken a few instants after the onset of a start-up flow with $\dot{\gamma} = 50$ s^{-1}. The last picture (t=30 s after the onset of shear) is representative of the asymptotic state.

to locally modify the proportion of the high shear rate band. In other words, α becomes a function of the position along the vorticity axis : $\alpha = \alpha(z)$. This feedback between the secondary flows and the shear-banded base flow is what allowed us to extract the dynamics of the secondary flows from the dynamics of the oscillations of the interface between bands, *i.e.* the oscillations of $\alpha(z)$ [37]. This correspondence between the dynamics of $\alpha(z)$ and the dynamics of secondary flows works as long as the secondary flows do not disrupt the band structure completely, remixing the two bands together. For systems in C_3, turbulent bursts can have such disrupting effects.

By studying systems over a wide range of parameters, we realize that several features of the asymptotic flows can depend crucially on the particulars of the feedback between the band structure and secondary flows. For instance, the behavior of the amplitude of the oscillations of the interface between bands most likely follows from a balance between the intensity of secondary flows deforming the interface and the effective surface tension of the interface, which can be connected to the stress diffusion coefficient [12]. In some cases, if the surface tension of the interface is not high enough (corresponding to very thin interfaces [12]), the high shear rate band can locally disappear in regions of strong radial inward flow. We observed this in systems with very high concentrations of surfactant. Those systems are concentrated and close to the isotropic/nematic (I/N) transition at equilibrium [4]. For instance, Fig. 10 gives the behavior of

the band structure and secondary flows developing in a system of 20 wt % of CTAB without salt in D_2O, at T=37.5°C in a TC cell with $\Lambda = 0.08$. This system has been widely studied in the last twenty years [18–22], in particular recently, by Helgeson *et al.* [23, 45]. Right after the onset of shear, the bands form, with a flat interface between them. Then, quickly, the interface starts to undulate, under the effect of the emerging vortex flow. But the resistance of the interface to those secondary flows is too weak and the proportion of the high shear rate band goes to zero in regions of inward radial flow. Eventually, the two bands seem to be mixed in regions of weak outward radial flow. We have observed similar behaviors at other temperatures, well into the nematic state (T=34°C) and further away from the I/N transition (T=44°C). The same phenomenology holds for a solution of [CTAB]=0.7 M and [NaNO$_3$]=0.3 M at T=30°C, in the TC cell with $\Lambda = 0.08$. This solution is also close to the I/N transition. The addition of salt switches the I/N transition towards higher concentrations [4].

Note that if shear-banding flows are in C_2 or C_3, the proportion of the high shear rate band is a function of the location along the vorticity direction but is also a function of time–because of the spatiotemporal dynamics of the vortex flow are often time-dependent (*cf.* fig. 6). This fact calls for a re-evaluation of experimental situations where the so-called 'vorticity banding' was observed [88–93]. Note moreover that the 'non-monotonic shear-thickening flow curve' underlying vorticity banding could be simply due to the emergence of secondary flows responsible for the increased resistance to flow. In sum, vorticity banding could very well originate from a constitutive instability [94]. But it could also be the consequence of secondary flows developing on top of a gradient banding base flow.

We did not study in detail the feedback between secondary flows and the spatiotemporal structure of the inhomogeneity of the shear rate leading to bands, but we believe that it can be an important aspect of other phenomena observed in flows of surfactant solutions. When the surfactant solutions are semi-dilute, concentrated, maybe even nematic, and present a clear banded structure along the gradient direction y, the present article and its grounds on previous studies show that the feedback is indeed crucial to the understanding of many 'fluctuating behaviors'. But the literature on flows of surfactant solutions is also very rich on the side of dilute solutions and their shear-thickening rheology [13]. We believe that considering the influence of elastic instabilities in some of those cases could be enlightening. Note however, that since the viscosity of dilute solutions is usually small, the full spectrum of inertio-elastic effects [62] may have to be considered on top of the kinetics of shear-induced structures [13]. In all cases, the effects of concentration fluctuations could also complicate the picture [51, 84–86]. The most general case where elasticity, inertia and shear-induced structural transitions and concentration fluctuations are taken into account is most likely chaotic. This
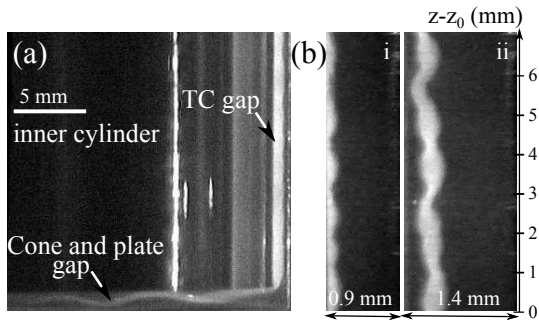
FIG. 11: (a) Large angle view of the bottom of the TC cell with $\Lambda = 0.04$. [CTAB]=0.3 M, [NaNO$_3$]=0.4 M, T=32°C, $\dot{\gamma} = 150$ s^{-1}. The bright white vertical line on the cylinder is due to a reflection of the laser sheet. (b) Pictures of the gap of a TC device with off-centered cylinders. [CTAB]=0.3 M, [NaNO$_3$]=0.4 M, T=30°C, $\Lambda \simeq 0.04$. Pictures (i) and (ii) are separated by 1 s.

is what had been coined *rheochaos* [5, 87].

It is worth acknowledging that by studying the elastic instability of shear-banded flows in TC geometry, we have greatly restricted the bounds of the feedback between secondary flows and the banding structure. The fact that the high shear rate band always occupies the locus of highest curvature greatly stabilizes the banding structure of the band against secondary flows. Except when secondary flows are turbulent, we do not observe a switch in the radial position of the high and low shear rate domains. But other base flows can allow much more freedom on the location of the bands. Theoretically, in a plane Couette flow (simple shear) the interfaces between bands can be located anywhere in the gap. In a cone and plate geometry, the high shear rate band can be located on the cone or plate, or even in the middle [32, 52, 95]. Fig. 11a shows the location of the bands at a given instant at the bottom of the TC device used in this article. The inner cylinder actually possesses a conical bottom end (Mooney-Couette). Thus the gap at the bottom of the Couette cell is a cone-and-plate geometry. As another example, Fig. 11b shows the band structure in a TC cell with the two cylinders slightly off-centered (by $\simeq 0.25$ mm). In both cases, the shape is highly unsteady. It is clear in those two cases that the feedback between secondary flows and the band structure leads to a much more complicated situation, witnessed by the geometrical complexity of the shape of the turbid band itself.

E.   Interfacial modes and axisymmetry

Note that if the instability of the base flow is solely due to the purely elastic instability of the high shear rate band, as described in section II B, then for small enough proportions of the high shear rate band, the flow should always be stable, no matter how high Λ and Wi_h are. In other words, $\lim_{\alpha \to 0} \Sigma = 0$. In all the conditions tested,

we have never observed this stable range. One reason is that the smallest width we can measure with our optical set-up is of the order of 50 μm. But another reason is that other instability mechanisms may be important for small bands.

So far, we have only considered an elastic instability arising in the bulk of the high shear rate band. It is a 'bulk mechanism', in the sense that it involves the value of a dimensionless quantity taken *in a domain*– here the band of width αd. Similarly, the homogeneous purely elastic instability in polymer solutions, or the inertial TC instability for Newtonian fluids, are bulk mechanisms. Another important class of instabilities involve 'interfacial mechanisms'. The Rayleigh-Taylor or Kelvin-Helmholtz instabilities are well known examples of interfacial mechanisms involving inertia. Interfacial mechanisms are not linked to the value of a dimensionless quantity taken in a domain, but to a dimensionless quantity linked to a difference in properties between domains separated by an interface. For instance, interfacial mechanisms involving inertia are usually linked to a difference in density between domains or even to a difference in Reynolds numbers.

It has long been known that viscoelastic materials can be subject to interfacial instability mechanisms involving elasticity [56]. The interface and bulk mechanisms are both 'elastic instabilities', in the sense that they are driven by normal stresses [56]. Indeed, before experiments suggested that shear-banding base flows in TC geometry could exhibit secondary flows structured along the vorticity axis, a linear stability analysis of the Johnson-Segalman model in simple shear suggested that shear-banding flows could become unstable along the flow direction x, due to an interfacial mechanism [27]. Fielding showed that a jump in the first normal stress difference between the bands could generate *interfacial modes* in the flow direction. Eventually, Fielding also investigated the stability of shear-banded flows subjected to perturbations along the vorticity direction z. She also found an instability, this time triggered by a jump in the second normal stress difference between bands [28]. It was shown that the instability of the interface generated recirculation rolls resembling Taylor-like vortices. Experiments done in straight micro-channels gave evidence that these interfacial modes along the vorticity direction dominated over the interfacial modes along the flow direction [96]. It is known that the bulk modes are linearly stable in base flows without curvature, *i.e.* for $\Lambda = 0$ [58]. At this point, it remained unclear which mechanism–bulk or interfacial–was responsible for the secondary flows and undulations of the interface between bands in TC flows.

But in a recent study, Fielding extended her original calculations focused on simple shear, to the case of TC flows [29]. She suggested that the interfacial and bulk elastic modes lie in two separate regions of the space $(\Lambda, N_1|_h)$, *i.e.* of the space (Λ, Wi_h) [29]. The bulk mode prevails at high Wi_h and high curvature Λ. The interfacial mode prevails at low Wi_h and low Λ. Nonethe-

less, only axisymmetric perturbations were considered in Fielding's study [29], and the stability analysis was performed for a single value of α. In the last theoretical study known to us, Nicolas and Morozov extended the stability analysis to non-axisymmetric modes [30]. They found that, for parameters corresponding to our earlier experiments on the CTAB/NaNO$_3$ system [35–38], the interfacial modes only dominate at the very beginning of the shear-banding regime ($\alpha \ll 1$). Bulk modes otherwise dominate. This last study significantly altered the stability diagram in the space (Λ,Wi_h) proposed by Fielding [29], because it showed that at a given value of $\Lambda = 0.08$, there was not any interval of parameters separating interfacial and bulk modes. The two types of modes can even interact with each other.

An extension of Nicolas and Morozov's study to TC flows with different Λ and different Wi_h would be necessary to substantiate this claim, but we believe that interfacial modes are only relevant when the effective curvature of the high shear rate band is low, *i.e.* when $\alpha\Lambda$ is small. We think that in our experiments, the zig-zag pattern in the spatiotemporal dynamics of secondary flows may be due to the dominance of the interfacial mode. Generally, the particulars of the spatiotemporal dynamics of secondary flows may be connected to interactions between bulk and interfacial modes.

Note that whether the non-axisymmetry originates from bulk or interfacial modes, we do not observe it in our experiments. Some non-axisymmetry can be a consequence of the spatiotemporal dynamics of vortex flows, but the main instability always seems to be along the vorticity direction rather than along the flow direction. A recent study by Decruppe *et al.* [97] has shown some evidence for non-axisymmetric modes. They studied a system made of [CTAB]=0.05 M and 0.1 M and [NaSal]=0.1 M, at T=23°C in a TC cell with $\Lambda = 0.5/28.5 \simeq 0.02$. An azimuthal instability seemed to occur, with a high shear rate band periodically moving in the middle of the gap. We have reproduced those experiments, seeing indeed what seems to be azimuthal modes, but entangled with other phenomena: turbidity fluctuations, some instability along the vorticity axis and elastic turbulence. A thorough investigation of the possibility of non-axisymmetric mode is left for further study.

IV. CONCLUSION AND PERSPECTIVES

In this article, we have shown that the TC flows of shear-thinning semi-dilute surfactant solutions are characterized by the convergence of two nonlinearities that have nothing to do with inertia–the source of nonlinearity in Newtonian fluids. We call the first nonlinearity 'structural'. Flows of surfactant solutions become inhomogeneous when for $Wi \sim 1$, we have $\sigma_{xy}/G_0 \lesssim 1$ [4]. In theoretical modelling this is often expressed as a condition on the ratio of the viscosity at infinite shear rate and the zero-shear viscosity $\eta \equiv \eta_\infty/\eta_0$, where $\eta_0 \equiv G_0\lambda$ [5].

Shear-banding occurs if $\eta < \eta_c$, for instance $\eta_c = 1/8$ for the Johnson-Segalman model [5, 12, 33]. In a TC flow with only the inner cylinder rotating, the domains of high shear rate form a band of width αd near the inner cylinder. The new base flow is a shear-banded base flow. It is influenced by wall slip [12, 39], but most importantly by the second nonlinearity. We call this second nonlinearity '*elastic*' [98]. In a TC flow of a fluid that lacks the first structural nonlinearity, like Boger fluids [2, 56, 58], or in simple models like the upper convected Maxwell model or Oldroyd-B model, the elastic nonlinearity leads to the emergence of secondary flows, first vortex flows, eventually turbulent flows. In small gap and with only the inner cylinder rotating, secondary flows emerge for $\Sigma_e \gtrsim 1$. Similarly, in the same shearing conditions, for the flow of shear-thinning semi-dilute surfactant solutions, the elastic nonlinearity leads to the emergence of secondary flows. If $\eta < \eta_c$ and $\alpha \neq 1$, then secondary flows are mainly localized in the band of width αd, if $\Sigma \gtrsim 1$. The secondary flows are first coherent (vortex flow) and eventually become turbulent. Otherwise secondary flows occupy the entire gap if $\Sigma_e \gtrsim 1$. In this case, secondary flows appear to be mostly turbulent. For more general cases, see the various subsections in section III.

The convergence of the structural and elastic nonlinearities demonstrated in this article calls for a precision to bring to a general concept running deep under our understanding of non-Newtonian fluids flows. In the field of soft matter, almost by definition, we study the feedback between the structure of a fluid and its flow. The flow can influence the structure. But the structure, even just by its elasticity, can influence the flow. Our study brings up one possible asymptotic solution of this feedback mechanism. But the general conclusion is that if we talk about the 'feedback between flow and structure' we must consider 'secondary flows' as well.

In general, if one is faced with the flow of a non-Newtonian fluid, the particular outcome of the feedback between flow and structure in a given geometry can be investigated by the convergence of the answers to the following questions:

1) What is the base flow for $Wi \sim 0$ and $Re \sim 0$? (*i.e.* the *linear regime.*)

2a) When does the base flow become *hydrodynamically unstable*, elastically via Wi, inertially via Re, or both?

2b) When does the base flow become *structurally unstable*? The very general criteria recently developed by Moorcroft and Fielding could be particularly instrumental in finding the answer to this question [99].

3) If 2a or 2b lead to a laminar flow, this laminar flow is the new base flow. Then ask again questions 2a and 2b.

This reaches much beyond the case of semi-dilute surfactant solutions. Note that the elastic nonlinearity should be present in any fluid with viscoelasticity, *i.e.* any fluid that has a non-zero first normal stress difference [2, 41]. This represents a very large class of materi-

als. Elastic instabilities have been shown in polymer solutions and now in surfactant solutions. Notwithstanding the proximity between surfactant solutions and polymer solutions, the elastic instability phenomenology was only recently brought to help the understanding of the former. This fact calls for a greater awareness of the emergence and effects of secondary flows on non-Newtonian fluids in general: foams, emulsions, colloidal suspensions, etc [2]. The fact that secondary flows have been shown to emerge in only a handful of non-Newtonian fluids may come from two different reasons. On the one hand, many non-Newtonian fluids can be both hydrodynamically unstable and structurally unstable. The interactions of the two nonlinearities may be unfavourable to secondary flows in many cases. It is known that a second difference of normal stresses can kill the elastic instability if it is of opposite sign to the first normal stress difference [56]. On the other hand, secondary flows in many non-Newtonian fluids are yet to be probed.

In any case, the development of new experimental apparatus allowing a better grip at the spatiotemporal dynamics of flows is essential.

To conclude back on surfactant solutions–our 'model system' [1], let us mention one recent progress which transcends the discussion of the present paper. Something that is even unclear in the case of elastic instabilities in polymer solutions is the role of elongation and stagnation in elastic instability mechanisms [100]. A few recent studies around polymer solutions recently drew the attention of the community toward flows with curved streamlines but that are dominated by extension rather than shear. The milestone is the discovery of purely elastic bifurcation in the cross-slot geometry by Arratia *et al.* [101]. Subsequent numerical simulations of viscoelastic models confirmed this instability [102, 103]. A similar instability has also been seen in micellar fluids, where the presence of shear-banding seems to affect the nature of the transition [104–107]. Surfactant solutions would not be constructive model systems if they were not always slightly more complicated than expected.

Fluctuating gradient and vorticity banding, elastic instability and elastic turbulence, bulk and interfacial modes, shear-thinning and shear-thickening, shear induced structures and concentration fluctuations, and rheochaos : We hope that this article has helped to advance the convergence of phenomena we associated to those words, and the understanding we gain from it.

[1] H. Rehage H. Hoffmann, *Molecular Physics* **74**, 933-973 (1991).

[2] R.G. Larson, The Structure and Rheology of Complex Fluids, Oxford University Press (1999).

[3] J.N. Israelachvili, Intermolecular and Surface Forces, London, Academic Press (1992).

[4] J.F. Berret, Rheology of wormlike micelles : Equilibrium properties and shear-banding transition, Molecular gels, Springer Netherlands, 667-720 (2006).

[5] M.E. Cates and S.M. Fielding, *Advances in Physics* **55**, 799-879 (2006).

[6] J.F. Berret, D.C. Roux and G. Porte, *J Phys II (France)* **4**,1261-1279 (1994).

[7] J.F. Berret, *Langmuir* **13**,2227-2234 (1997).

[8] J.F. Berret, G. Porte and J.P. Decruppe *Phys. Rev. E* **55**,1668-1676 (1997).

[9] G. Porte, J.F. Berret and J.L. Harden, *Journal de Phys. II* **7** 459-472 (1997).

[10] J.F. Berret and G. Porte, *Phys. Rev. E* **60**,4268-4271 (1999).

[11] P.D. Olmsted, *Rheol. Acta* **47**, 283-300 (2008).

[12] M.A. Fardin *et al.*, *Soft Matter* **8**, 910-922 (2012).

[13] S. Lerouge and J.F. Berret, Shear-induced transitions and instabilities in surfactant wormlike micelles, *Adv. Polym. Sci.*, **230**, 1-71 (2010).

[14] Salmon, J. B. and Colin, A. and Manneville, S. and Molino, F., *Phys. Rev. Lett.* **90**, 228303 (2003).

[15] Lopez-Gonzalez, M. R. and Holmes, W. M. and Callaghan, P. T., *Soft Matter* **2**, 865-869 (2006).

[16] Holmes, W. M. and Lopez-Gonzalez, M. R. and Callaghan, P. T., *Eur. Phys. Lett.* **64**, 274-280 (2003).

[17] Lopez-Gonzalez, M. R. and Holmes, W. M. and Callaghan, P. T. and Photinos, P. J., *Phys. Rev. Lett.* **93**, 268302 (2004).

[18] Bécu, L. and Manneville, S. and Colin, A., *Phys. Rev. Lett.* **93**, 018301 (2004).

[19] Bécu, L. and Anache, D. and Manneville, S. and Colin, A., *Phys. Rev. E* **76**, 011503 (2007).

[20] Cappelaere, E. and Berret, J.-F. and Decruppe, J. P. and Cressely, R. and Lindner, P., al, *Phys. Rev. E* **56**, 1869-1878 (1997).

[21] Fischer, E. and Callaghan, P. T., *Eur. Phys. Lett.* **50**,803-809 (2000).

[22] Fischer, E. and Callaghan, P. T., *Phys. Rev. E* **64**, 011501 (2001).

[23] M.E. Helgeson, M.D. Reichert, Y.T. Hu, and N.J. Wagner, *Soft Matter* **5**, 3858-3869 (2009).

[24] M.P. Lettinga and S. Manneville, *Phys. Rev. Lett.* **103**, 248302 (2009).

[25] Feindel, K. and Callaghan, P.T., *Rheol. Acta* **49**, 1003-1013 (2010).

[26] Fielding, S. M. and Olmsted, P. D.,*Phys. Rev. Lett.* **96**, 104502 (2006).

[27] S.M. Fielding, *Phys. Rev. Lett.* **95**, 134501 (2005).

[28] S.M. Fielding, *Phys. Rev. E* **76**, 016311 (2007).

[29] S. M. Fielding, *Phys. Rev. Lett.* **104**, 198303 (2010).

[30] A. Nicolas and A. Morozov, *Phys. Rev. Lett.* **108**, 088302 (2012).

[31] S. Manneville, *Rheol. Acta* **47**, 301-318 (2008).

[32] P.T. Callaghan, *Rheol. Acta* **47**, 243-255 (2008).

[33] S.M. Fielding, *Soft Matter* **2**,1262-1279 (2007).

[34] M.A. Fardin S. Lerouge, *Eur. Phys. J. E* (submitted).

[35] S. Lerouge *et al.*, *Phys. Rev. Lett.* **96**, 088301 (2006).

[36] S. Lerouge *et al.*, *Soft Matter* **4**, 1808-1819 (2008).

[37] M.A. Fardin *et al.*, *Phys. Rev. Lett.* **103**, 028302 (2009).

[38] M.A. Fardin *et al.*, *Phys. Rev. Lett.* **104**, 178303 (2010).

[39] M.A. Fardin *et al.*, *Soft Matter* **8**, 2535-2553 (2012).

[40] M.A. Fardin *et al.*, *Eur. Phys. Lett.* **96**, 44004 (2011).

[41] R.B. Bird, R.C. Armstrong and O. Hassager, Dynamics of Polymeric Liquids: Volume 1, John Wiley & Sons, Inc. (1987).

[42] E. Cappelaere R. Cressely, *Colloid. Polym. Sci.* **275**, 407-418 (1997).

[43] Decruppe, J. P. and Greffier, O. and Manneville, S. and Lerouge, S., *Phys. Rev. E* **73**, 061509 (2006).

[44] Raudsepp, A. and Callaghan, P. T., *Soft Matter* **4**, 784-796 (2008).

[45] M.E. Helgeson, P.A. Vasquez, E.W. Kaler, and N.J. Wagner, *J. Rheol.* **53**, 727-756 (2009).

[46] J.M. Dealy, *Rheol. Bul.* **79**, 2 (2010).

[47] O. Radulescu *et al*, *Europhys. Lett.* **62**, 230-236 (2003).

[48] O. Radulescu and P.D. Olmsted, *Rheol. Acta* **38**, 606-613 (1999).

[49] C-Y.D. Lu, P.D. Olmsted and R.C. Ball, *Phys. Rev. Lett.* **84**, 642-645 (2000).

[50] O. Radulescu and P.D. Olmsted, *J. non-Newt. Fluid Mech.* **91**, 141-162 (2000).

[51] V. Schmitt, C.M. Marques and F. Lequeux, *Phys. Rev. E* **52**, 4009 (1995).

[52] C.J. Dimitriou, L. Casanellas, T.J. Ober G.H. McKinley, *Rheol. Acta* DOI 10.1007/s00397-012-0619-9 (2012).

[53] S. Manneville, L. Bécu, and A. Colin, *Eur. Phys. J. AP* **28**, 361-373 (2004).

[54] A. Groisman V. Steinberg, *Phil. Mag.* B **78**, 253-263 (1998).

[55] R.G. Larson, E.S.J. Shaqfeh S.J. Muller, *J. Fluid Mech.* **218**, 573-600 (1990).

[56] R.G. Larson, *Rheol. Acta* **31**, 213-263 (1992).

[57] P. Pakdel and G.H. McKinley, *Phys. Rev. Lett.* **77**, 2459-2462 (1996) and G.H. McKinley *et al.*, *J. Non-Newt. Fluid Mech.* **67**, 19-48 (1996).

[58] A.N. Morozov W. van Saarloos, *Physics Reports* **447**, 112-143 (2007).

[59] S. Chandrasekhar, Hydrodynamic and Hydromagnetic Stability, Dover, New York (1981).

[60] G.I. Taylor, *Phil. Trans. Royal Society* A **223**, 289-343 (1923).

[61] R.E. Khayat, *J. Fluid Mech.* **400**, 33-58 (1999).

[62] S.J. Muller, *Korea-Australia Rheol. J.* **20**, 117-125 (2008).

[63] C.S. Dutcher and S.J. Muller, *Phys. Rev. E* **75**, 047301 (2007).

[64] A. Esser and S. Grossmann, *Phys. Fluids* **8**, 1814 (1996).

[65] C.D. Andereck, S.S. Liu and H.L. Swinney, *J. Fluid Mech.* **164**, 155-183 (1986).

[66] R. Tagg, *Nonlinear Sci. Today* **4**, 1-25 (1994).

[67] M. Avgousti and A.N. Beris, *J. Non Newtonian Fluid Mech.* **50**, 225 (1993).

[68] B.M. Baumert and S.J. Muller, *Rheol. Acta* **34**, 147-159 (1995).

[69] B.M. Baumert and S.J. Muller, *Phys. Fluids* **9**, 566-586 (1997).

[70] B.M. Baumert and S.J. Muller, *J. non-Newt. Fluid Mech.* **83**, 33-69 (1999).

[71] J.M. White and S.J. Muller, *J. Rheol.* **47**, 1467 (2003).

[72] U.A. Al-Mubaiyedh, R. Sureshkumar and B. Khomami, *Phys. Fluids* **14**, 1056 (2002).

[73] A. Groisman and V. Steinberg, *Phys. Rev. Lett.* **78**, 1460-1463 (1997).

[74] A. Groisman and V. Steinberg, *Phys. Fluids* **10**, 2451-2463 (1998).

[75] K.A. Kumar and M.D. Graham, *Phys. Rev. Lett.* **85**, 4056-4059 (2000).

[76] K.A. Kumar and M.D. Graham, *J. Fluid Mech.* **443**, 301-328 (2001).

[77] M. Lange and B. Eckhardt, *Phys. Rev. E* **64**, 027301 (2001).

[78] D.G. Thomas, R. Sureshkumar and B. Khomami, *Phys. Rev. Lett.* **97**, 054501 (2006).

[79] D.G. Thomas, U.A. Al-Mubaiyedh, R. Sureshkumar and B. Khomami, *J. non-Newt. Fluid Mech.* **138**, 111-133 (2006).

[80] A. Groisman and V. Steinberg, *Phys. Rev. Lett.* **77**, 1480-1483 (1996).

[81] O. Crumeyrolle, I. Mutabazi and M. Grisel, *Phys. Fluids* **14**, 1681-1688 (2002).

[82] C. Masselon, J. B. Salmon and A. Colin, *Phys. Rev. Lett.* **100**, 038301 (2008).

[83] C. Masselon, A. Colin and P. Olmsted, *Phys. Rev. E* **81**, 021502 (2010).

[84] S.M. Fielding and P.D. Olmsted, *Eur. Phys. J. E* **11**, 65-83 (2003).

[85] R. Ganapathy, A.K. Sood, *Phys. Rev. Lett.* **96**, 108301 (2006).

[86] M.E. Helgeson, L. Porcar, C. Lopez-Barron, and N.J. Wagner, *Phys. Rev. Lett.* **105**, 084501 (2010).

[87] M.E. Cates, D.A. Head and A. Ajdari, *Phys. Rev. E* **66**, 025202 (2002).

[88] Fischer, P., *Rheol. Acta* **39**, 234-240 (2000).

[89] Fischer, P. and Wheeler, E. K. and Fuller, G. G., *Rheol. Acta* **41**, 35-44 (2002).

[90] Herle, V. and Fischer, P. and Windhab, E. J., *Langmuir* **21**, 9051-9057 (2005).

[91] Herle, V. and Manneville, S. and Fischer, P. and Windhab, E. J., *Eur. Phys. J. E* **26**, 3-12 (2008).

[92] Kang, K. G. and Lettinga, M. P. and Dogic, Z. and Dhont, J. K. G., *Phys. Rev. E* **74**, 026307 (2006).

[93] J.K.G. Dhont W.J. Briels, *Rheol Acta* **47**, 257-281 (2008).

[94] J.L. Goveas P.D. Olmsted, *Eur. Phys. J. E* **6**, 79-89 (2001).

[95] Britton, M. M. and Callaghan, P. T., *Phys. Rev. Lett.* **78**, 4930-4933 (1997).

[96] P. Nghe, S.M. Fielding, P. Tabeling and A. Ajdari, *Phys. Rev. Lett.* **104**, 248303 (2010).

[97] J.P. Decruppe, L. Bécu, O. Greffier and N. Fazel, *Phys. Rev. Lett.* **105**, 258301 (2010).

[98] Of course, the elasticity of materials also has to do with their structure, but 'quasi-linearly', in the sense that the nonlinear *elastic* terms in the equations of motion are present as soon as the first normal stress difference is non-zero, even when the fluid has a constant viscosity independent of shear rate, like in Boger fluids, or in the upper convected Maxwell model or Oldroyd B model. By 'structural nonlinearity', we assume more complex behaviors probably involving some kind of underlying

plasticity.

[99] R.L. Moorcroft and S.M. Fielding, arXiv:1201.6259v1 [cond-mat.soft].

[100] M.A. Fardin and A. Morozov, Colloquium: Flow instabilities and turbulence in viscoelastic fluids, summary of the workshop organized in July 2010, in the Lorentz Centre, Leiden (in preparation).

[101] P.E. Arratia *et al.*, *Phys. Rev. Lett.* **96**, 144502 (2006).

[102] R.J. Poole *et al.*, *Phys. Rev. Lett.* **99**, 164503 (2007); G.N. Rocha *et al.*, *J. Non-Newt. Fluid Mech.* **156**, 58-69 (2009).

[103] L. Xi and M.D. Graham, *J. Fluid Mech.* **622**, 145-165 (2009).

[104] J.A. Pathak and S.D. Hudson, *Macromolecules* **39**, 8782-8792 (2006).

[105] S.J. Haward *et al.*, *Soft Matter* **8**, 536-555 (2012).

[106] S.J. Haward, and G.H. McKinley, *Phys. Rev. E* **85** 031502(14) (2012).

[107] T.J. Ober, J. Soulages and G.H. McKinley, *J. Rheol.* **55**, 1127-1159 (2011).